AASE 81-232

APPROXIMATE FACTORIZATION FOR INCOMPRESSIBLE FLOW

(NASA-CR-164668) APPROXIMATE FACTORIZATION FOR INCOMPRESSIBLE FLOW Ph.D. Thesis (Mississippi State Univ., Mississippi State.) 106 p HC A06/MF A01 CSCL 20D

N81-29383

Unclas
G3/34 27172

By

ROBERT S. BERNARD

A Dissertation
Submitted to the Faculty of
Mississippi State University
in Partial Fulfillment of the Requirements
for the Degree of Doctor of Philosophy
in the College of Engineering

Mississippi State, Mississippi

August 1981

APPROXIMATE FACTORIZATION FOR INCOMPRESSIBLE FLOW

By

ROBERT S. BERNARD

A Dissertation
Submitted to the Faculty of
Mississippi State University
in Partial Fulfillment of the Requirements
for the Degree of Doctor of Philosophy
in the College of Engineering

Mississippi State, Mississippi

August 1981

APPROXIMATE FACTORIZATION
FOR INCOMPRESSIBLE FLOW

By

Robert S. Bernard

J. F. Thompson
Professor of Aerospace
Engineering (Chairman of
Committee and Dissertation
Director)

Z. U. A. Warsi
Professor of Aerospace
Engineering (Member of
Committee)

Keith Koenig
Assistant Professor of
Aerospace Engineering
(Member of Committee)

C. Wayne Mastin
Professor of Mathematics
(Member of Committee)

Hugh W. Coleman
Associate Professor of
Mechanical Engineering
(Member of Committee)

Charles B. Cliett
Professor and Head of the
Department of Aerospace
Engineering

A. L. McDaniel
Dean of the College of
Engineering

Marvin T. Loftin
Vice President for Graduate
Studies and Research

August 1981

For

Bettye, Doug, and Bailey

ACKNOWLEDGEMENTS

My long-standing indebtedness to Joe Thompson is now compounded with this dissertation, which would never have been written without his counsel and support. Some of the others who helped me survive the operation are listed below, in no particular order.

Contributors	Contributions
Kyle Cooper	Hard Facts & Software
Pat Roache	Boundary Conditions
Keith Koenig, Dave Whitfield, & Doctor Warsi	Conversational Fluid Dynamics
Charles Cliett	Financial & Moral Support
Bettye Douglas	Room & Board
Mike Freeman	Literary Criticism
Anutosh Moitra	Linguistic Consultation
John Ziebarth	Fishing Tips
Denice Heath	Typing & Editing
Gay Goodnite	Artwork
Bob Rohani, Crofton Sloan, & Guy Jackson	Instigation
Fran Cunningham	Not Moving to Wyoming
Mister Jiggs	Protection

Also, I am financially grateful to the U.S. Army Engineer Waterways Experiment Station, who supported me throughout my course work, and to the Langley Research Center, who supported my research under NASA Grant NCR-25-001-005.

Thank You.

Bob Bernard
Mississippi State University
August 1981

ABSTRACT

ROBERT S. BERNARD, Doctor of Philosophy, 1981

Major: Engineering, Department of Aerospace Engineering

Title of Dissertation: Approximate Factorization for Incompressible Flow

Directed by: Dr. Joe F. Thompson

Pages in Dissertation: 92 Words in Abstract: 250

Abstract

The technique of approximate factorization (AF) , as formulated by Beam and Warming, is employed for computational solution of the incompressible Navier-Stokes equations. In each time step, the AF algorithm is used to solve the vectorized momentum equation in delta form, based on the pressure calculated in the previous time step. The newly-calculated velocities are substituted into the pressure equation (obtained from a linear combination of the continuity and momentum equations), which is then solved by means of line SOR.

The combined AF/SOR algorithm is developed for arbitrary curvilinear coordinates in two dimensions, but can easily be extended to three. The coordinates used for computation are the body-fitted coordinates of Thompson et al., generated numerically by the more recent method of Thompson and Mastin.

Computational results are presented for the NACA 66_3018 airfoil at Reynolds numbers of 1000 and 40,000 and attack angles of 0 and 6 degrees. Comparison with wind-tunnel data for Re = 40,000 indicates good qualitative agreement between measured and calculated pressure distributions. Quantitative agreement is only fair, however, with the

calculations somewhat displaced from the measurements. Furthermore, the computed velocity profiles are unrealistically thick around the airfoil, due to the excessive amount of artificial viscosity needed for stability.

Based on the performance of the algorithm with regard to stability, it is concluded that AF/SOR is suitable for calculations at Reynolds numbers less than 10,000. Speedwise, the method is faster than point SOR by at least a factor of two.

TABLE OF CONTENTS

NOMENCLATURE

Symbols†

C_p	Pressure Coefficient
$\underset{\sim}{g}$	Body-Force Vector or Freestream Pressure Gradient, Eq. (6.1)
J	Jacobian of Coordinate Transformation, Eq. (3.18)
p	Pressure
q	Vectorized Velocity, Eq. (4.5)
Re	Reynolds Number
t	Time
$\underset{\sim}{u}$	Velocity Vector, Eq. (1.1)
u	x-Component of Velocity
v	y-Component of Velocity
x,y	Cartesian Coordinates
ξ,η	Curvilinear Coordinates
δ	Divergence of $\underset{\sim}{u}$, unless stated otherwise
μ	Dynamic Viscosity
μ_T	Eddy Viscosity
ε	Artificial Viscosity Coefficient, Eq. (7.3)
α	Angle of Attack
ω	Acceleration Parameter for Line SOR

Superscripts

n	Time-Step Index
(m)	Iteration Count

---

† This is a list of symbols that appear throughout the text. Specialized symbols and definitions are explained in full wherever they are used.

Subscripts

$(\ )_t$	Partial Derivative with respect to t
$(\ )_x$	Partial Derivative with respect to x
$(\ )_y$	Partial Derivative with respect to y
$(\ )_\xi$	Partial Derivative with respect to ξ
$(\ )_\eta$	Partial Derivative with respect to η
$(\ )_{ij}$	Evaluation of ( ) at finite-difference node point, $\xi=i$ and $\eta=j$, unless stated otherwise

Operators

Δ	Time-Increment Operator, Eq. (4.27)
∇	Gradient Operator
$\nabla\cdot\underset{\sim}{u}$	Divergence of $\underset{\sim}{u}$

LIST OF FIGURES

Figure | Page

CHAPTER I

INTRODUCTION

Since the late 1960's, computational fluid dynamics (CFD) has evolved as a distinct branch of fluid mechanics, due to numerous advances in computer technology and numerical methodology. Now, with the increasing cost of fuel and hardware and the decreasing cost of electronic calculation, CFD offers a viable alternative to laboratory testing. Chapman [1] gives a concise overview of the state-of-the-art (as of 1979), summarizing its past development as well as its prognosis for the future.

Computational solutions of the Reynolds-averaged Navier-Stokes equations date back to the early 1970's. At first the machine-time requirement was prohibitive, and calculations were restricted to simple geometries and low Reynolds numbers. These initial limitations were greatly reduced, however, with the development of improved algorithms such as MacCormack's rapid solver [2] and effective grid-generation techniques such as the body-fitted coordinates of Thompson et al. [3]. Further reduction of the machine-time requirement was achieved when Beam and Warming [4] and Briley and McDonald [5] independently formulated the technique of approximate factorization (AF).

The AF algorithm is an alternating-direction implicit (ADI) scheme, suitable for partial differential equations of the parabolic/hyperbolic type. Although it requires more computer storage than other methods, it is also much faster, maintaining second-order accuracy with one iteration per time step. Furthermore, since it is fully implicit, AF is not subject to the restrictive time-step limitation that impedes explicit methods.

To date, approximate factorization has been successfully employed in a number of applications involving supersonic, transonic, and compressible subsonic flow [6, 7, 8]. Except for the work of Steger and Kutler [9], however, there seems to have been no published calculation for incompressible flow. This is not surprising, since the incompressible equations of motion are not amenable to the AF algorithm, at least not without some modification.

The spatial factorization used in the ADI scheme requires that each of the governing equations contain a time derivative. Unfortunately, the time derivative in the continuity equation is lost in the incompressible limit. Steger and Kutler circumvent this difficulty artificially by adding a pressure time derivative to the continuity equation:

$$\frac{\partial p}{\partial t} + \beta \nabla \cdot \underset{\sim}{u} = 0 \tag{1.1}$$

where $\beta >> 1$ so that $\nabla \cdot \underset{\sim}{u} \to 0$ as the flow approaches the steady state. The calculated transient flow is, however, only asymptotically correct, since Eq. (1.1) is a fabrication and not a true equation of motion.

Available methods for calculating transient incompressible flow seem expensive and inefficient compared to those for the compressible case, especially considering that the incompressible equations are "simpler". One is forced to choose between explicit techniques, limited to small time steps, and implicit techniques, requiring many iterations. The very existence of an efficient algorithm such as approximate factorization prompts one to think that an equally efficient recipe might be possible for incompressible flow. That, at least, was the motivation for the investigation reported herein.

The AF technique will not accomodate the incompressible continuity equation without a time derivative. Nevertheless, it is quite applicable for the incompressible momentum equation as long as the pressure is specified by some other means. The implementation of separate algorithms for the momentum and continuity equations allows one to take advantage of approximate factorization for the velocity calculation but still requires some sort of iterative solver for the pressure. This also precludes the simultaneous calculation of velocity and pressure, so that the combined method is not fully implicit.

In order to investigate the utility of a two-phase solver based on approximate factorization, the two-dimensional incompressible momentum equation[†] in conservative form is first transformed from cartesian coordinates to arbitrary curvilinear coordinates. The transformed equation is discretized by means of a three-point backward difference in time and central difference in space, so that the difference operator can be factored into a product of two unidirectional operators. The factored difference equation is then solved in an ADI sequence with the aid of a direct inversion for each of the two coordinate directions. Throughout this entire process, the pressure is assumed to have been previously calculated.

A Poisson equation for the pressure is obtained from a linear combination of the continuity and momentum equations. After discretization

---

[†] The terms "momentum equation" and "Navier-Stokes equations" are interchangeable for incompressible flow.

with central difference approximations, successive over-relaxation by lines (line SOR) is used to solve the pressure equation. Line SOR was chosen as the pressure algorithm because it facilitates the implicit treatment of Neumann boundary conditions.

The body-fitted coordinate system is generated numerically for a single-element airfoil using the method described in Thompson and Mastin [10]. Subsequent calculations for the velocity and pressure are executed in the transformed plane, rather than the physical plane, on a 113 x 51 rectangular grid with unit mesh spacing. Due to the one-to-one mapping between the physical and transformed planes, the recovery and presentation of results in the physical plane is straightforward.

A linear gradual start, equivalent to a uniform body force or static pressure gradient, is used to accelerate the flow from rest to its ultimate freestream velocity. At each time step the (explicit) pressure solver is executed first, based on velocities from the previous time step. Then the (implicit) AF momentum solver is executed, generating velocity increments for the current time step.

An algebraic turbulence model, formulated by Baldwin and Lomax [14], is employed for calculating eddy viscosity in the Reynolds-averaged momentum equation. In addition, an artificial viscosity, proportional to the divergence of the velocity, is appended to the physical viscosity in order to help dissipate numerical oscillations.

The foregoing paragraphs summarize the form and content of the AF/SOR method. The questions to be addressed are:

1. Is this method stable and accurate for the same Reynolds numbers and time increments attainable with conventional implicit methods such as point SOR?

2. What are its limitations in terms of high Reynolds number, time-step size, and boundary conditions?

3. Under what circumstances is the method preferable to conventional implicit methods?

The answers are given in Chapter IX.

CHAPTER II

EQUATIONS OF MOTION IN CARTESIAN COORDINATES

2.1. Navier-Stokes Equations

Newton's Second Law (conservation of momentum), applied to the fluid inside an arbitrary material volume V, takes the mathematical form

$$\int_V \frac{\partial}{\partial t}(\rho u_i)dV + \int_S (\rho u_i)u_j n_j dS = \int_S (\Sigma_{ij} - p\delta_{ij})n_j dS + \int_V \rho g_i dV \tag{2.1}$$

Equation (2.1) represents the well-known Navier-Stokes equations in their integral form. The index "i" denotes any of the three cartesian directions, x_1, x_2, x_3, and the Einstein summation convention has been employed for the index "j". The dimensional variables are

ρ = density

u_i = velocity

S = material surface

n_i = unit vector, normal to S

Σ_{ij} = shear stress tensor

p = pressure

δ_{ij} = Kronecker delta

g_i = body-force acceleration, due to gravity, non-inertial coordinate system, etc.

The divergence theorem transforms Eq. (2.1) to

$$\begin{aligned}&\int_V \frac{\partial}{\partial t}(\rho u_i)dV + \int_V \frac{\partial}{\partial x_j}(\rho u_i u_j)dV \\ &\quad = \int_V \left(\frac{\partial}{\partial x_j}\Sigma_{ij} - \frac{\partial p}{\partial x_i} + \rho g_i\right)dV\end{aligned} \tag{2.2}$$

From a computational standpoint, the integral relation (2.2) is probably the most important of the many possible forms of the Navier-Stokes equations. In order to achieve a meaningful representation of Newton's second law, numerical simulations should begin with Eq. (2.2), preserving the integral form as accurately as possible.

Since the volume V is arbitrary, the integral operators can be removed from Eq. (2.2), leaving only the relation between the integrands, which is

$$\frac{\partial}{\partial t}(\rho u_i) + \frac{\partial}{\partial x_j}(\rho u_i u_j) = \frac{\partial}{\partial x_j}\Sigma_{ij} - \frac{\partial p}{\partial x_i} + \rho g_i \tag{2.3}$$

For an incompressible fluid the density is constant, so Eq. (2.3) becomes

$$\frac{\partial u_i}{\partial t} + \frac{\partial}{\partial x_j}(u_i u_j) = \frac{1}{\rho}\left(\frac{\partial}{\partial x_j}\Sigma_{ij} - \frac{\partial p}{\partial x_i}\right) + g_i \tag{2.4}$$

and Stokes's Law gives the shear stress as

$$\Sigma_{ij} = \mu\left(\frac{\partial u_i}{\partial x_j} + \frac{\partial u_j}{\partial x_i}\right) \tag{2.5}$$

where μ is the viscosity of the fluid.

At this point it is expedient to nondimensionalize Eqs. (2.4) and (2.5). Accordingly, the dimensional variables are now replaced by their nondimensional counterparts:

$$\hat{u}_i = u_i/U_\infty \tag{2.6}$$

$$\hat{x}_i = x_i/\ell \tag{2.7}$$

$$\hat{t} = tU_\infty/\ell \tag{2.8}$$

$$\hat{\mu} = \mu/\mu_\infty \tag{2.9}$$

$$\hat{p} = p/(\rho U_\infty^2) \tag{2.10}$$

$$\hat{g}_i = g_i \ell/U_\infty^2 \tag{2.11}$$

The reference quantities are

U_∞ = freestream velocity

ℓ = characteristic length (in this case, airfoil chord)

μ_∞ = freestream viscosity

Combining Eqs. (2.4) and (2.5) with (2.6) - (2.11) the dimensionless Navier-Stokes equations for incompressible flow are

$$\frac{\partial \hat{u}_i}{\partial \hat{t}} + \frac{\partial}{\partial \hat{x}_j}(\hat{u}_i \hat{u}_j) = -\frac{\partial \hat{p}}{\partial \hat{x}_i} + \hat{g}_i + \frac{1}{Re}\frac{\partial}{\partial \hat{x}_j}\left[\hat{\mu}\left(\frac{\partial \hat{u}_i}{\partial \hat{x}_j} + \frac{\partial \hat{u}_j}{\partial \hat{x}_i}\right)\right] \tag{2.12}$$

where Re is the Reynolds number, given by

$$Re = \frac{\rho U_\infty \ell}{\mu_\infty} \tag{2.13}$$

The viscosity is a material constant for incompressible, nonconducting fluids. It is retained here as a variable, however, in order to facilitate the implementation of an algebraic model for turbulence.

2.2 Continuity Equation

In addition to the Navier-Stokes equations for conservation of momentum, all fluids must obey the continuity equation, which expresses conservation of mass:

$$\int_V \frac{\partial \rho}{\partial t}\, dV + \int_S \rho u_j n_j \, dS = 0 \tag{2.14}$$

Applying the divergence theorem and eliminating the volume integrals as before, Eq. (2.14) reduces to

$$\frac{\partial \rho}{\partial t} + \frac{\partial}{\partial x_j}(\rho u_j) = 0 \tag{2.15}$$

which, for incompressible fluids, is simply

$$\frac{\partial u_j}{\partial x_j} = 0 \tag{2.16}$$

Equation (2.16) is unchanged by the introduction of nondimensional variables.

2.3 Nondimensional Equations of Motion in Two Dimensions

From this point on, all variables used will be nondimensional, and the circumflex (^) will be dropped from the notation. Identifying x, y, u, v with x_1, x_2, u_1, u_2 respectively, the equations of motion for incompressible flow in two dimensions are[†]

$$u_t + (p + u^2)_x + (uv)_y = \frac{1}{Re}[2(\mu u_x)_x + (\mu u_y)_y + (\mu v_x)_y] \tag{2.17}$$

$$v_t + (uv)_x + (p + v^2)_y = \frac{1}{Re}[(\mu u_y)_x + (\mu v_x)_x + 2(\mu v_y)_y] \tag{2.18}$$

$$u_x + v_y = 0 \tag{2.19}$$

Equations (2.17) and (2.18) represent the x- and y- components of the momentum equation (2.12), and Eq. (2.19) replaces the continuity equation (2.20). The subscripts x, y, and t indicate x-, y-, and t-derivatives. The conservative form (see section 3.2) has been retained in (2.17) and (2.18) to preserve the integral relation (2.2) in the finite-difference algorithm.

[†] In the absence of a body force.

CHAPTER III

CURVILINEAR COORDINATES

3.1 Coordinate Generation

Whenever a physical problem is to be solved by analytical means, one of the first steps is the choice of an expedient coordinate system - preferably one that will exploit any symmetries and keep the boundary conditions simple. If a problem yields an exact solution, it is usually because there exists a coordinate system in which the governing equations are algebraically tractable.

From a computational standpoint, geometry is equally important. Moreover, except for some additional bookkeeping, the formulation of difference equations is no more difficult in curvilinear coordinates than it is in cartesian coordinates. The practical obstacle is the fact that engineering problems seldom involve shapes for which coordinate systems can be specified analytically. Thus the difficulty is mainly one of finding or generating a coordinate system with boundaries that match the physical boundaries.

Thompson et al. [3] have developed a method of grid generation whereby coordinate systems can be specified for arbitrary geometries. Consider, for example, an airfoil cross-section in two dimensions (Figure 1). The desired curvilinear coordinates, ξ and η , should have the following properties:

1. The coordinates ξ and η must be single-valued functions of the cartesian coordinates x and y.
2. Extrema in ξ and η may occur only on the boundaries, or on a branch cut, where the values of both coordinates are specified. (In this case η is fixed and ξ varies along the airfoil surface).

Now it happens that the desired properties of ξ and η are the same as those of solutions to elliptic partial differential equations with Dirichlet boundary conditions. The simplest of these is Laplace's equation, which allows the values of ξ and η to be specified at will along the boundaries. A more useful equation, however, is Poisson's equation, which facilitates control of both the mesh spacing and the cell aspect ratio. Thus lines of constant ξ and/or η can be densely concentrated in regions where large physical gradients are expected.

In two dimensions, a system of two Poisson equations must be solved to obtain ξ(x,y) and η(x,y):

$$\xi_{xx} + \xi_{yy} = -\frac{\alpha_c}{J_c^2} P(\xi,\eta) \tag{3.1}$$

$$\eta_{xx} + \eta_{yy} = -\frac{\gamma_c}{J_c^2} Q(\xi,\eta) \tag{3.2}$$

Depending on their magnitude and spatial variation, the attraction functions P(ξ,η) and Q(ξ,η) can be used to concentrate coordinate lines about a given point or curve. Since the numerical boundary conditions can be incorporated more accurately in the rectangular ξη-plane (Figure 1), it is expedient to solve the transformed system of equations:

$$\alpha_c x_{\xi\xi} - 2\beta_c x_{\xi\eta} + \gamma_c x_{\eta\eta} = -(\alpha_c x_\xi P + \gamma_c x_\eta Q) \tag{3.3}$$

$$\alpha_c y_{\xi\xi} - 2\beta_c y_{\xi\eta} + \gamma_c y_{\eta\eta} = -(\alpha_c y_\xi P + \gamma_c y_\eta Q) \tag{3.4}$$

Although Eqs. (3.3) and (3.4) are more complicated than (3.1) and (3.2), computation is far simpler on the rectangular grid. The coefficients in Eqs. (3.1) - (3.4) are themselves functions of ξ and η, given below:

$$\alpha_c = x_\eta^2 + y_\eta^2 \tag{3.5}$$

$$\beta_c = x_\xi x_\eta + y_\xi y_\eta \tag{3.6}$$

$$\gamma_c = x_\xi^2 + y_\xi^2 \tag{3.7}$$

$$J_c = x_\xi y_\eta - x_\eta y_\xi \tag{3.8}$$

Equations (3.3) and (3.4) are solved by point SOR after the attraction functions have been specified. The procedure for Q is [10]:

$$r(\eta) = r_J + \frac{G(\eta) - 1}{G(\eta) + 1}\left(1 - \frac{r_1}{r_J}\right)b \tag{3.9a}$$

$$G(\eta) = \left(\frac{b + r_J}{b - r_J}\right)^{\left(\frac{\eta - J}{J - 1}\right)} \tag{3.9b}$$

$$Q(\xi,\eta) = -\frac{\gamma_c}{J_c^2}\left(\frac{r''}{r'} - \frac{r'}{r}\right) \tag{3.10}$$

with b chosen so as to produce a specified value of $r'(1)$. The first η-line (η=1) represents the body, and r_1 is one-half chord length (the radius of a circle circumscribing the airfoil cross-section). The quantity r_J is the radius of a circle tangent to the outer boundary, η=J. In the solution of Eq. (3.2), the effect of Q defined by Eqs. (3.9) and (3.10) is to position the line η=N at a distance roughly equal to $r_N - r_1$ from the body. For the second η-line (η=2), this is about 1% of the boundary-layer thickness for the Blasius flat plate solution, i.e.,

$$r'(1) = r_2 - r_1 = 0.01\left(\frac{5}{\sqrt{Re}}\right) \tag{3.11}$$

3.2 Coordinate Transformation

In Chapter II, the dimensionless Navier-Stokes equations (2.17) and (2.18) are given in physically conservative form. That is, derivatives such as $(u^2)_x$ are not expanded into the analytically equivalent form

$$(u^2)_x = 2uu_x \tag{3.12}$$

The reason for this decision is that finite-difference approximations for the conservative expressions are consistent with the integral form of the Navier-Stokes equations (2.2), while those for the nonconservative expressions are not. Roache demonstrates this at length in his book [11]. Suffice it here to say that the conservative form is generally safer for computational work.

A similar consideration arises when the Navier-Stokes equations are to be transformed from cartesian coordinates to curvilinear coordinates. If the chain rule alone is used to expand derivatives such as

$$u_x = \xi_x u_\xi + \eta_x u_\eta \tag{3.13}$$

then the finite-difference equations will be inconsistent with the integral Navier-Stokes equations. Thus it is important that the transformation rule be geometrically conservative in the sense that Eqs. (2.17) and (2.18) are physically conservative. The transformation given below has the desired property [8].

Let A_1, A_2, A_3 be the components of the vector $\underset{\sim}{A}$ in cartesian coordinates (x_1, x_2, x_3). Employing the Einstein summation convention, the divergence of $\underset{\sim}{A}$ in curvilinear coordinates (ξ_1, ξ_2, ξ_3) then takes the form

$$\frac{\partial A_i}{\partial x_i} = J \frac{\partial \hat{A}_i}{\partial \xi_i} \tag{3.14}$$

where

$$\hat{A}_i = \frac{1}{J} \frac{\partial \xi_i}{\partial x_j} A_j \tag{3.15}$$

and J denotes the Jacobian†

$$J = \frac{\partial(\xi_1,\xi_2,\xi_3)}{\partial(x_1,x_2,x_3)} \tag{3.16}$$

In Chapters IV and V the two-dimensional coordinates x_i and ξ_i are

$$\begin{aligned} x_1 &= x \qquad\qquad & \xi_1 &= \xi \\ x_2 &= y \qquad\qquad & \xi_2 &= \eta \end{aligned} \tag{3.17}$$

and the Jacobian is

$$J = \begin{vmatrix} \xi_x & \xi_y \\ \eta_x & \eta_y \end{vmatrix} = \xi_x\eta_y - \xi_y\eta_x \tag{3.18}$$

Applying Eqs. (3.14), (3.15), (3.17), and (3.18) in two dimensions, the divergence of $\underset{\sim}{A}$ becomes

$$\frac{\partial A_1}{\partial x} + \frac{\partial A_2}{\partial y} = J\left(\frac{\partial \hat{A}_1}{\partial \xi} + \frac{\partial \hat{A}_2}{\partial \eta}\right) \tag{3.19}$$

where

$$\hat{A}_1 = \frac{1}{J}(\xi_x\, A_1 + \xi_y\, A_2) \tag{3.20}$$

$$\hat{A}_2 = \frac{1}{J}(\eta_x\, A_1 + \eta_y\, A_2) \tag{3.21}$$

---

† The Jacobian J is not to be confused with the maximum η-value (η=J) in section 3.1.

The x- or y- derivative of a scalar is the same as the divergence of a vector with only one component; for example,

$$u_x = J(\hat{u}_\xi + \hat{v}_\eta) \tag{3.22}$$

$$\hat{u} = \frac{\xi_x u}{J} \tag{3.23}$$

$$\hat{v} = \frac{\eta_x u}{J} \tag{3.24}$$

Second derivatives should be calculated via a combination of the chain rule (3.13) and the transformation (3.14), as shown in the example below

$$u_{xx} = (u_x)_x \tag{3.25}$$

$$(u_x)_x = J[(\hat{u}_x)_\xi + (\hat{v}_x)_\eta] \tag{3.26}$$

$$\hat{u}_x = \frac{\xi_x\, u_x}{J} = \frac{\xi_x}{J}(\xi_x\, u_\xi + \eta_x\, u_\eta) \tag{3.27}$$

$$\hat{v}_x = \frac{\eta_x\, u_x}{J} = \frac{\eta_x}{J}(\xi_x\, u_\xi + \eta_x\, u_\eta) \tag{3.28}$$

Note that Eq. (3.13) has been substituted for u_x in Eqs. (3.27) and (3.28), since only the <u>outside</u> derivative in (3.26) need employ the transformation (3.14) to preserve the integral relation (2.2).

CHAPTER IV

SOLUTION OF THE NAVIER-STOKES EQUATIONS IN CURVILINEAR COORDINATES

4.1. Transformed Equations

Using the transformation (3.14) for an arbitrary coordinate system, the x- and y- momentum equations (2.17) and (2.18) can be expressed as a single vector equation:

$$\frac{1}{J}\frac{\partial q}{\partial t} + \frac{\partial}{\partial \xi} A(q) + \frac{\partial}{\partial \eta} B(q) = \frac{\partial}{\partial \xi}[Wq_\xi + Xq_\eta] + \frac{\partial}{\partial \eta}[Yq_\xi + Zq_\eta] \quad (4.1)$$

where

$$\xi = \xi(x,y) \quad (4.2)$$

$$\eta = \eta(x,y) \quad (4.3)$$

$$J = \xi_x \eta_y - \xi_y \eta_x \neq 0 \quad (4.4)$$

$$q = \begin{bmatrix} u \\ v \end{bmatrix} \quad (4.5)$$

$$A(q) = \begin{bmatrix} a_1(q) \\ a_2(q) \end{bmatrix} \quad (4.6)$$

$$B(q) = \begin{bmatrix} b_1(q) \\ b_2(q) \end{bmatrix} \quad (4.7)$$

$$W = \begin{bmatrix} w_{11} & w_{12} \\ w_{21} & w_{22} \end{bmatrix} \quad (4.8)$$

$$X = \begin{bmatrix} x_{11} & x_{12} \\ x_{21} & x_{22} \end{bmatrix} \quad (4.9)$$

$$Y = \begin{bmatrix} y_{11} & y_{12} \\ y_{21} & y_{22} \end{bmatrix} \quad (4.10)$$

$$Z = \begin{bmatrix} z_{11} & z_{12} \\ z_{21} & z_{22} \end{bmatrix} \tag{4.11}$$

The individual components of the vectors (4.6) and (4.7) and matrices (4.8) - (4.11) are as follows:

$$a_1(q) = \frac{1}{J}[\xi_x(p + u^2) + \xi_y uv] \tag{4.12}$$

$$a_2(q) = \frac{1}{J}[\xi_x uv + \xi_y(p + v^2)] \tag{4.13}$$

$$b_1(q) = \frac{1}{J}[\eta_x(p + u^2) + \eta_y uv] \tag{4.14}$$

$$b_2(q) = \frac{1}{J}[\eta_x uv + \eta_y(p + v^2)] \tag{4.15}$$

$$w_{11} = \tilde{\mu}(2\xi_x^2 + \xi_y^2) \tag{4.16}$$

$$w_{12} = w_{21} = \tilde{\mu}\xi_x\xi_y \tag{4.17}$$

$$w_{22} = \tilde{\mu}(\xi_x^2 + 2\xi_y^2) \tag{4.18}$$

$$x_{11} = y_{11} = \tilde{\mu}(2\xi_x\eta_x + \xi_y\eta_y) \tag{4.19}$$

$$x_{12} = y_{21} = \tilde{\mu}\xi_y\eta_x \tag{4.20}$$

$$x_{21} = y_{12} = \tilde{\mu}\xi_x\eta_y \tag{4.21}$$

$$x_{22} = y_{22} = \tilde{\mu}(\xi_x\eta_x + 2\xi_y\eta_y) \tag{4.22}$$

$$z_{11} = \tilde{\mu}(2\eta_x^2 + \eta_y^2) \tag{4.23}$$

$$z_{12} = z_{21} = \tilde{\mu}\eta_x\eta_y \tag{4.24}$$

$$z_{22} = \tilde{\mu}(\eta_x^2 + 2\eta_y^2) \tag{4.25}$$

where

$$\tilde{\mu} = \frac{\mu}{\mathrm{Re}\ J} \tag{4.26}$$

4.2. Temporal Discretization

Following the procedure of Beam and Warming [4], the momentum equation (4.1) is now discretized in time. Using the superscript "n" to denote a particular time step, the time increment of q is

$$\Delta q^n = q^{n+1} - q^n \tag{4.27}$$

The 3-point backward-difference expression for $\partial q/\partial t$ is

$$\left(\frac{\partial q}{\partial t}\right)^{n+1} = \frac{3q^{n+1} - 4q^n + q^{n-1}}{2\Delta t} + O(\Delta t^2) \tag{4.28}$$

Incorporation of Eqs. (4.27) and (4.28) into (4.1) leads to

$$\frac{\Delta q^n}{J} = \frac{1}{3}\,\frac{\Delta q^{n-1}}{J} - \frac{2}{3}\,\Delta t\left[\frac{\partial}{\partial \xi} A(q) + \frac{\partial}{\partial \eta} B(q)\right]^{n+1}$$

$$+ \frac{2}{3}\,\Delta t\left\{\frac{\partial}{\partial \xi}[Wq_\xi + Xq_\eta]^{n+1} + \frac{\partial}{\partial \eta}[Yq_\xi + Zq_\eta]^{n+1}\right\} \tag{4.29}$$

$$+ O(\Delta t^3)$$

Since A(q) and B(q) are independent of q_ξ and q_η, it follows that

$$\frac{\partial A}{\partial \xi}^{n+1} = \frac{\partial A}{\partial \xi}^{*} + P^n \Delta q_\xi^n + O(\Delta t^2) \tag{4.30}$$

$$\frac{\partial B}{\partial \eta}^{n+1} = \frac{\partial B}{\partial \eta}^{*} + Q^n \Delta q_\eta^n + O(\Delta t^2) \tag{4.31}$$

where

$$A^* = A(q^n\ ;\ p^{n+1}) \tag{4.32}$$

$$B^* = B(q^n\ ;\ p^{n+1}) \tag{4.33}$$

$$P = \frac{\partial A}{\partial q} = \begin{bmatrix} p_{11}(q) & p_{12}(q) \\ p_{21}(q) & p_{22}(q) \end{bmatrix} \tag{4.34}$$

$$Q = \frac{\partial B}{\partial q} = \begin{bmatrix} q_{11}(q) & q_{12}(q) \\ q_{21}(q) & q_{22}(q) \end{bmatrix} \tag{4.35}$$

and

$$p_{11}(q) = \frac{1}{J}(2\xi_x u + \xi_y v) \tag{4.36}$$

$$p_{12}(q) = \frac{\xi_y u}{J} \tag{4.37}$$

$$p_{21}(q) = \frac{\xi_x v}{J} \tag{4.38}$$

$$p_{22}(q) = \frac{1}{J}(\xi_x u + 2\xi_y v) \tag{4.39}$$

$$q_{11}(q) = \frac{1}{J}(2\eta_x u + \eta_y v) \tag{4.40}$$

$$q_{12}(q) = \frac{\eta_y u}{J} \tag{4.41}$$

$$q_{21}(q) = \frac{\eta_x v}{J} \tag{4.42}$$

$$q_{22}(q) = \frac{1}{J}(\eta_x u + 2\eta_y v) \tag{4.43}$$

Now, assuming that μ_T is a slowly varying function of time, it is admissible to replace Eq. (4.29) by

$$\begin{aligned} \frac{\Delta q^n}{J} = \frac{1}{3}\frac{\Delta q^{n-1}}{J} &+ \frac{2}{3}\Delta t\,\frac{\partial}{\partial \xi}[W^n \Delta q_\xi^n + X^n \Delta q_\eta^n - P^n \Delta q^n] \\ &+ \frac{2}{3}\Delta t\,\frac{\partial}{\partial \eta}[Y^n \Delta q_\xi^n + Z^n \Delta q_\eta^n - Q^n \Delta q^n] \\ &+ \frac{2}{3}\Delta t\{\frac{\partial}{\partial \xi}[W^n q_\xi^n + X^n q_\eta^n - A^*] + \frac{\partial}{\partial \eta}[Y^n q_\xi^n + Z^n q_\eta^n - B^*]\} \\ &+ O(\Delta t^3) \end{aligned} \tag{4.44}$$

Following Beam and Warming, the cross derivatives are time-lagged in Eq. (4.44) using the substitutions

$$\frac{\partial}{\partial\xi}(X\Delta q_\eta^n) = \frac{\partial}{\partial\xi}(X\Delta q_\eta^{n-1}) + O(\Delta t^2) \tag{4.45}$$

$$\frac{\partial}{\partial\eta}(Y\Delta q_\xi^n) = \frac{\partial}{\partial\eta}(Y\Delta q_\xi^{n-1}) + O(\Delta t^2) \tag{4.46}$$

The other derivatives of Δq_ξ^n, Δq_η^n, and Δq^n are moved to the left side of (4.44), resulting in

$$\begin{aligned}\frac{\Delta q^n}{J} - \frac{2}{3}\Delta t\frac{\partial}{\partial\xi}(W\Delta q_\xi^n - P^n\Delta q^n) - \frac{2}{3}\Delta t\frac{\partial}{\partial\eta}(Z\Delta q_\eta^n - Q^n\Delta q^n)\\ = \frac{1}{3}\frac{\Delta q^{n-1}}{J} + \frac{2}{3}\Delta t\frac{\partial}{\partial\xi}(Wq_\xi^n + Xq_\eta^* - A^*)\\ + \frac{2}{3}\Delta t\frac{\partial}{\partial\eta}(Yq_\xi^* + Zq_\eta^n - B^*) + O(\Delta t^3)\end{aligned} \tag{4.47}$$

where

$$q^* = q^n + \Delta q^{n-1} \tag{4.48}$$

4.3. Approximate Spatial Factorization

After multiplying through by J, the left side of (4.47) is factored into a product of ξ- and η- operations, leaving the following sequence of equations to be solved:

$$\begin{aligned}\overline{\Delta q} + D_\xi((P^n - W\frac{\partial}{\partial\xi})\overline{\Delta q}) = \frac{1}{3}\Delta q^{n-1} + D_\xi(Wq_\xi^n + Xq_\eta^* - A^*)\\ + D_\eta(Yq_\xi^* + Zq_\eta^n - B^*)\end{aligned} \tag{4.49}$$

$$\Delta q^n + D_\eta((Q^n - Z\frac{\partial}{\partial\eta})\Delta q^n) = \overline{\Delta q} + O(\Delta t^3) \tag{4.50}$$

where

$$D_\xi = \frac{2}{3}J\Delta t\frac{\partial}{\partial\xi} \tag{4.51}$$

$$D_\eta = \frac{2}{3}J\Delta t\frac{\partial}{\partial\eta} \tag{4.52}$$

4.4. Spatial Discretization

Spatial discretization of Eqs. (4.49) and (4.50) is accomplished by means of the central-difference expressions given in Appendix A. After some regrouping of terms, the spatial difference equations representing (4.49) and (4.50) take the form:†

$$\begin{aligned}
&-(\tilde{P}^n_{i-1,j} + 3\tilde{W}^n_{i-1,j} + \tilde{W}^n_{i+1,j})\overline{\Delta q}_{i-1,j} + [I + 4(\tilde{W}^n_{i-1,j} + \tilde{W}^n_{i+1,j})]\overline{\Delta q}_{ij} \\
&\qquad +(\tilde{P}^n_{i+1,j} - 3\tilde{W}^n_{i+1,j} - \tilde{W}^n_{i-1,j})\overline{\Delta q}_{i+1,j} \\
&\qquad = \frac{1}{3}\Delta q^{n-1}_{ij} - (\tilde{A}^*_{i+1,j} - \tilde{A}^*_{i-1,j}) - (\tilde{B}^*_{i,j+1} - \tilde{B}^*_{i,j-1}) \\
&+(3\tilde{W}^n_{i-1,j} + \tilde{W}^n_{i+1,j})q^n_{i-1,j} - 4(\tilde{W}^n_{i-1,j} + \tilde{W}^n_{i+1,j})q^n_{ij} + (3\tilde{W}^n_{i+1,j} + \tilde{W}^n_{i-1,j})q^n_{i+1,j} \\
&+(3\tilde{Z}^n_{i,j-1} + \tilde{Z}^n_{i,j+1})q^n_{i,j-1} - 4(\tilde{Z}^n_{i,j-1} + \tilde{Z}^n_{i,j+1})q^n_{ij} + (3\tilde{Z}^n_{i,j+1} + \tilde{Z}^n_{i,j-1})q^n_{i,j+1} \\
&\quad + \tilde{X}^n_{i+1,j}(q^*_{i+1,j+1} - q^*_{i+1,j-1}) - \tilde{X}^n_{i-1,j}(q^*_{i-1,j+1} - q^*_{i-1,j-1}) \\
&\quad + \tilde{Y}^n_{i,j+1}(q^*_{i+1,j+1} - q^*_{i-1,j+1}) - \tilde{Y}^n_{i,j-1}(q^*_{i+1,j-1} - q^*_{i-1,j-1})
\end{aligned} \tag{4.53}$$

and

$$\begin{aligned}
&-(\tilde{Q}^n_{i,j-1} + 3\tilde{Z}^n_{i,j-1} + \tilde{Z}^n_{i,j+1})\Delta q^n_{i,j-1} + [I + 4(\tilde{Z}^n_{i,j-1} + \tilde{Z}^n_{i,j+1})]\Delta q^n_{ij} \\
&\qquad +(\tilde{Q}^n_{i,j+1} - 3\tilde{Z}^n_{i,j+1} - \tilde{Z}^n_{i,j-1})\Delta q^n_{i,j+1} = \overline{\Delta q}_{ij}
\end{aligned} \tag{4.54}$$

where

$$\tilde{P}^n = \frac{\Delta t}{3} J_{ij} P^n \tag{4.55}$$

$$\tilde{Q}^n = \frac{\Delta t}{3} J_{ij} Q^n \tag{4.56}$$

---

† The subscripts "i" and "j" are indices for finite-difference mesh points, with $\xi=i$, $\eta=j$, and $\Delta\xi=\Delta\eta=1$.

$$\tilde{W}^n = \frac{\Delta t}{6} J_{ij} W^n \tag{4.57}$$

$$\tilde{X}^n = \frac{\Delta t}{6} J_{ij} X^n \tag{4.58}$$

$$\tilde{Y}^n = \frac{\Delta t}{6} J_{ij} Y^n \tag{4.59}$$

$$\tilde{Z}^n = \frac{\Delta t}{6} J_{ij} Z^n \tag{4.60}$$

$$I = \begin{bmatrix} 1 & 0 \\ 0 & 1 \end{bmatrix} \tag{4.61}$$

Note that in Eqs. (4.55) - (4.60) the indices of J_{ij} are held fixed; e.g.,

$$\tilde{P}^n_{i+1,j} = \frac{\Delta t}{3} J_{ij} P^n_{i+1,j} \tag{4.62}$$

4.5. ADI Sequence

Equations (4.53) and (4.54) in sequence resemble one iteration of an alternating-direction implicit (ADI) scheme. First Eq. (4.53) is solved on each line of constant η (constant j); then Eq. (4.54) is solved on each line of constant ξ (constant i). Actually, Eq. (4.53) represents a set of linear equations for the values of $\overline{\Delta q}_{ij}$, where j is specified and i varies from 1 to I_{max}. The same applies to Eq. (4.54) for Δq^n_{ij}, but with i specified and j varying. In both cases the matrix operators occur in block-tridiagonal form, and the solutions can be obtained directly (i.e., without iteration) using the well-known Thomas algorithm [8,12]. For a known pressure distribution, only one ADI iteration is necessary to obtain the velocity distribution, correct to second order in time.

CHAPTER V

FORMULATION AND SOLUTION OF THE PRESSURE EQUATION

5.1. Conservation of Mass

There often arise situations in which volume changes are negligible compared with other phenomena. In particular, liquids and gases flowing at low Mach numbers exhibit essentially the same behavior as incompressible flow.

From a mathematical standpoint, incompressibility eliminates the equation of state, which relates pressure, volume, and temperature. As a result, the thermal and kinetic energies are decoupled, and the flow can be analyzed on a purely mechanical basis, without reference to thermodynamic effects.

Unfortunately, the incompressible equations of motion are somewhat inconvenient for computational solution because nowhere does there appear a time derivative of the pressure. Since there is no direct way of advancing the pressure in time, an indirect method must be formulated such that conservation of mass is always satisfied. In this regard, the continuity equation is a constraint that determines the instantaneous distribution of pressure throughout the flow field.

5.2. Formulation of the Pressure Equation

Taking the divergence of the momentum equation[†] in cartesian coordinates leads to

---

[†] The x-derivative of (2.17) plus the y-derivative of (2.18).

$$\delta_t + p_{xx} + p_{yy} + u_x^2 + v_y^2 + 2u_y v_x$$
$$= \frac{2}{Re}[\mu_x(u_{xx} + u_{yy}) + \mu_y(v_{xx} + v_{yy}) + \mu_{xx}u_x + \mu_{xy}(u_y + v_x) + \mu_{yy}v_y] \tag{5.1}$$

where

$$\delta = u_x + v_y \equiv 0 \tag{5.2}$$

In obtaining Eq. (5.1), it is assumed that $\delta=0$, but that $\delta_t \neq 0$. The δ_t is a correction term (ideally zero) recommended by Hirt and Harlow [13]. Note that Eq. (5.1) has been developed in nonconservative form, and δ has been extracted and set equal to zero. Following Roache [11], this can be taken one step further:

$$u_x^2 + v_y^2 = \delta^2 - 2u_x v_y \tag{5.3}$$

Combining Eqs. (5.2) and (5.3) with (5.1), the pressure equation in cartesian coordinates then becomes

$$p_{xx} + p_{yy} = - \delta_t + 2(u_x v_y - u_y v_x)$$
$$+ \frac{2}{Re}[\mu_x(u_{xx} + u_{yy}) + \mu_y(v_{xx} + v_{yy}) + \mu_{xx}u_x + \mu_{xy}(u_y + v_x) + \mu_{yy}v_y] \tag{5.4}$$

Equation (5.4) is an elliptic partial differential equation (PDE) that establishes the instantaneous relation between pressure and velocity everywhere in the fluid. Representing a linear combination of Eqs. (2.17) - (2.19), it is a restatement of conservation of mass, contingent upon conservation of momentum. Ideally it should be solved simultaneously with Eqs. (2.17) and (2.18), but the approach taken herein is to solve the momentum and pressure equations separately. The vector momentum equation is of the parabolic type, and the approximate-factorization algorithm described in Chapter IV is currently the most efficient technique available for parabolic-hyperbolic PDE's. On the other hand, the pressure equation is elliptic and is unsuited to the method of Chapter IV because it lacks a time derivative.

5.3. The Pressure Equation in Curvilinear Coordinates

Since Eq. (5.4) is an auxiliary constraint and not a conservation equation per se, some leeway is admissible concerning its transformation to curvilinear coordinates. Accordingly, the left-hand side is expressed in geometrically conservative form (section 3.2.), but the right-hand side is expressed in geometrically nonconservative form, using the chain rule. The resulting equation is:

$$\begin{aligned} J\{\frac{\partial}{\partial\xi}[\hat{W}p_\xi + \hat{X}p_\eta] + \frac{\partial}{\partial\eta}[\hat{X}p_\xi + \hat{Z}p_\eta]\} \\ = -\delta_t + 2(u_x v_y - u_y v_x) \\ + \frac{2}{Re}[\mu_x(u_{xx} + u_{yy}) + \mu_y(v_{xx} + v_{yy}) \\ + \mu_{xx}u_x + \mu_{xy}(u_y + v_x) + \mu_{yy}v_y] \end{aligned} \tag{5.5}$$

where

$$\hat{W} = \frac{1}{J}(\xi_x^2 + \xi_y^2) \tag{5.6}$$

$$\hat{X} = \frac{1}{J}(\xi_x\eta_x + \xi_y\eta_y) \tag{5.7}$$

$$\hat{Z} = \frac{1}{J}(\eta_x^2 + \eta_y^2) \tag{5.8}$$

and the derivatives on the right-hand side of (5.5) are evaluated as follows

$$f_x = \xi_x f_\xi + \eta_x f_\eta \tag{5.9}$$

$$f_y = \xi_y f_\xi + \eta_y f_\eta \tag{5.10}$$

$$f_{xx} = \xi_x (f_x)_\xi + \eta_x (f_x)_\eta \tag{5.11}$$

$$f_{xy} = \frac{1}{2}[\xi_y (f_x)_\xi + \eta_y (f_x)_\eta + \xi_x (f_y)_\xi + \eta_x (f_y)_\eta] \tag{5.12}$$

$$f_{yy} = \xi_y (f_y)_\xi + \eta_y (f_y)_\eta \tag{5.13}$$

Note that Eq. (5.12) is written such that $f_{xy} = f_{yx}$.

5.4. Temporal Discretization

Using a two-point backward-difference approximation for the time derivative,†

$$\delta_t^{n+1} = \frac{\delta^{n+1} - \delta^n}{\Delta t} + O(\Delta t) \tag{5.14}$$

the desired velocity field (u,v) at time level "n+1" must satisfy continuity, i.e.,

$$\delta^{n+1} = 0 \tag{5.15}$$

Due to numerical error, however, δ^n is never precisely zero. Thus the two-point backward-time approximation for Eq. (5.5) is

---

† Strictly speaking, a three-point (second-order) expression should be used to restrict the truncation error to $O(\Delta t^2)$, as in Chapter IV. This, in fact, was the original approach. After some computer experiments, however, it was found that the first-order pressure equation is much more stable, making truncation-error considerations academic.

$$
\begin{aligned}
J\{\frac{\partial}{\partial\xi}[\hat{W}p_{\xi}^{n+1} + \hat{X}p_{\eta}^{n+1}] + \frac{\partial}{\partial\eta}[\hat{X}p_{\xi}^{n+1} + \hat{Z}p_{\eta}^{n+1}]\}
&= \frac{\delta^{n}}{\Delta t} + 2(u_x v_y - u_y v_x)^{n+1} \\
&+ \frac{2}{Re}[\mu_x(u_{xx} + u_{yy}) + \mu_y(v_{xx} + v_{yy}) \\
&+ \mu_{xx}u_x + \mu_{xy}(u_y + v_x) + \mu_{yy}v_y]^{n+1} \\
&+ O(\Delta t)
\end{aligned}
\tag{5.16}
$$

In order to solve Eq. (5.16) for p^{n+1}, the velocity distribution $(u,v)^{n+1}$ must be known. Noting that

$$u^{n+1} = u^{n} + O(\Delta t) \tag{5.17}$$

$$v^{n+1} = v^{n} + O(\Delta t) \tag{5.18}$$

The velocity distribution $(u,v)^{n}$ can be substituted for $(u,v)^{n+1}$ in Eq. (5.16), preserving the instantaneous truncation error $O(\Delta t)$.

5.5. Spatial Discretization

As in Chapter IV, the viscosity μ is regarded as a slowly varying function of time, so that $\mu^{n+1} \approx \mu^{n}$. Using central-difference approximations for the spatial derivatives (Appendix A), the difference equation representing Eq. (5.16) is

$$
\begin{aligned}
&\hat{A}_{ij}p_{i-1,j}^{n+1} + \hat{B}_{ij}p_{ij}^{n+1} + \hat{C}_{ij}p_{i+1,j}^{n+1} + \hat{D}_{ij}p_{i,j-1}^{n+1} + \hat{E}_{ij}p_{i,j+1}^{n+1} \\
&+ \hat{G}_{ij}p_{i+1,j+1}^{n+1} + \hat{H}_{ij}p_{i-1,j+1}^{n+1} + \hat{K}_{ij}p_{i+1,j-1}^{n+1} + \hat{L}_{ij}p_{i-1,j-1}^{n+1} = F_{ij}
\end{aligned}
\tag{5.19}
$$

where

$$\hat{A}_{ij} = \frac{1}{4} J_{ij}(3\hat{W}_{i-1,j} + \hat{W}_{i+1,j}) \tag{5.20}$$

$$\hat{B}_{ij} = - J_{ij}(\hat{W}_{i-1,j} + \hat{W}_{i+1,j} + \hat{Z}_{i,j-1} + \hat{Z}_{i,j+1}) \tag{5.21}$$

$$\hat{C}_{ij} = \frac{1}{4} J_{ij}(3\hat{W}_{i+1,j} + \hat{W}_{i-1,j}) \tag{5.22}$$

$$\hat{D}_{ij} = \frac{1}{4} J_{ij}(3\hat{Z}_{i,j-1} + \hat{Z}_{i,j+1}) \tag{5.23}$$

$$\hat{E}_{ij} = \frac{1}{4} J_{ij}(3\hat{Z}_{i,j+1} + \hat{Z}_{i,j-1}) \tag{5.24}$$

$$\hat{G}_{ij} = \frac{1}{4} J_{ij}(\hat{X}_{i+1,j} + \hat{X}_{i,j+1}) \tag{5.25}$$

$$\hat{H}_{ij} = - \frac{1}{4} J_{ij}(\hat{X}_{i-1,j} + \hat{X}_{i,j+1}) \tag{5.26}$$

$$\hat{K}_{ij} = - \frac{1}{4} J_{ij}(\hat{X}_{i+1,j} + \hat{X}_{i,j-1}) \tag{5.27}$$

$$\hat{L}_{ij} = \frac{1}{4} J_{ij}(\hat{X}_{i-1,j} + \hat{X}_{i,j-1}) \tag{5.28}$$

and†

$$\begin{aligned} F_{ij} &= \frac{\delta^n_{ij}}{\Delta t} + 2(u^n_x v^n_y - u^n_y v^n_x)_{ij} \\ &+ \frac{2}{Re}[\mu^n_x(u^n_{xx} + u^n_{yy}) + \mu^n_y(v^n_{xx} + v^n_{yy}) \\ &+ \mu^n_{xx} u^n_x + \mu^n_{xy}(u^n_y + v^n_x) + \mu^n_{yy} v^n_y]_{ij} \end{aligned} \tag{5.29}$$

The x- and y-derivatives in Eq. (5.29) are evaluated using Eqs. (5.9) - (5.13), and the ξ- and η- derivatives appearing therein are calculated numerically from Eq. (A.1).

---

† Note that the quantity δ_{ij} represents here the divergence of velocity evaluated at ξ=i, η=j, and is not to be confused with the Kronecker delta used in Eq. (2.1).

5.6. Iterative Solution

Equation (5.19) represents a set of N linear equations in N unknowns (p_{ij}^{n+1}), where N is the total number of finite-difference node points in the flow field. For large N, direct solution is impractical and inaccurate, leaving indirect (iterative) methods as the more viable class of alternatives. Of the latter, successive over-relaxation by lines (line SOR) has been chosen as the method of preference, because it converges rapidly for elliptic equations with both Neumann and Dirichlet boundary conditions (see Chapter VI).

Dropping the superscript "n+1" and replacing it with "(m)", to denote the $m^{\underline{th}}$ iteration, the following equation is solved on each line of constant ξ (constant i):

$$\begin{aligned} & - \hat{D}_{ij} p^{*}_{i,j-1} - \hat{B}_{ij} p^{*}_{ij} - \hat{E}_{ij} p^{*}_{i,j+1} \\ & = - F_{ij} + \hat{A}_{ij} p^{(m-1)}_{i-1,j} + \hat{C}_{ij} p^{(m-1)}_{i+1,j} \\ & + \hat{G}_{ij} p^{(m-1)}_{i+1,j+1} + \hat{H}_{ij} p^{(m-1)}_{i-1,j+1} \\ & + \hat{K}_{ij} p^{(m-1)}_{i+1,j-1} + \hat{L}_{ij} p^{(m-1)}_{i-1,j-1} \end{aligned} \tag{5.30}$$

Equation (5.30) actually represents a set of linear equations for the value of p^{*}_{ij} at each value of j. The matrix operator for the left-hand side is point tridiagonal, so that Eq. (5.30) can be solved directly using the Thomas algorithm. Once the values of p^{*}_{ij} have been found on a given ξ-line, the values of $p^{(m)}_{ij}$ are calculated from

$$p_{ij}^{(m)} = \omega p_{ij}^{*} + (1 - \omega)p_{ij}^{(m-1)} \qquad (5.31)$$

where the acceleration parameter ω must lie between 0 and 2 for convergence.

The foregoing procedure is repeated for each ξ-line in succession, until the entire field has been swept. One sweep of the field constitutes a single iteration of line SOR.

CHAPTER VI

INITIAL VALUES AND BOUNDARY CONDITIONS

6.1. General Requirements

In order to obtain a unique solution for a system of partial differential equations, it is necessary to specify certain initial and boundary values for the unknown functions and their derivatives, depending on the type(s) of equations involved. In particular, for the incompressible Navier-Stokes equations, the initial velocity and pressure distributions must be given, and the velocity (or a spatial derivative thereof) must be specified on the physical boundaries at all times.

The no-slip condition for viscous flow sets the relative velocity at zero on all fixed impermeable boundaries (in this case the airfoil surface). Freestream velocities may be specified at will, subject to conservation of mass and momentum.

There is no self-evident boundary condition for the pressure, nor is one required in the strict sense. In fact, the pressure can be eliminated entirely by using a stream-function/vorticity formulation in two dimensions [11]. Nevertheless, when the primitive variables (u,v,p) are retained in the Navier-Stokes equations, and a Poisson equation is to be solved for the pressure, then a pressure boundary condition _is_ required.

6.2. Freestream Boundary

Ideally, the freestream (inflow/outflow) boundary lies an infinite distance from any obstacles in the flow. On a computational grid, "infinite" means far enough away that their effect on the flow is weak.

Here a freestream velocity or a freestream pressure gradient can be specified (one implies the other due to conservation of momentum) and the flow is usually presumed to be inviscid. When the upstream condition is that of uniform flow, it is customary to hold the velocity and pressure constant on the inflow boundary. On the outflow boundary, either the flow variables or their gradients may be specified.

6.3. Gradual Start

The inflow is accelerated from zero to its final velocity ($|\underset{\sim}{u}|_\infty = 1$) by imposing a uniform body force on the entire flow field. During this phase, the inflow velocity is given by

$$\underset{\sim}{u}_\infty = \int \underset{\sim}{g}\, dt \tag{6.1}$$

and the outflow boundary condition is

$$(\underset{\sim}{n}\cdot\nabla\underset{\sim}{u})_\infty = 0 \tag{6.2}$$

where $\underset{\sim}{n}_\infty$ is a vector normal to the outflow boundary. The freestream pressure condition is

$$\nabla p_\infty = 0 \tag{6.3}$$

and $\underset{\sim}{g}$ is a vector of uniform magnitude and direction, so that

$$\nabla\cdot\underset{\sim}{g} = 0 \tag{6.4}$$

Thus the pressure equation (5.5) is unaltered by the presence of $\underset{\sim}{g}$. When the acceleration phase is complete, the body force is of course

$$\underset{\sim}{g} = 0 \tag{6.5}$$

Since the freestream boundary is far from the airfoil, Eq. (6.3) can be replaced by the condition

$$p_\infty = 0 \tag{6.6}$$

The inflow velocity condition after the gradual start is

$$u_\infty = \cos \alpha \tag{6.7}$$

$$v_\infty = \sin \alpha \tag{6.8}$$

where α is the angle of attack.

The body force is equivalent to a freestream pressure gradient acting on the fluid, and it can be treated as such, both analytically and computationally. Thus the flow could be accelerated by adding a static pressure gradient to the right-hand side of the momentum equation. In any case, the body force influences the field pressure through the pressure boundary condition on the airfoil surface, regardless of the interpretation.

6.4. Pressure Boundary Condition

The no-slip condition requires that $\underset{\sim}{u} = 0$ on the body surface, so that the normal component of the momentum equation (including the body force) reduces to the nonconservative form

$$\underset{\sim}{n}\cdot\nabla p = \underset{\sim}{n}\cdot(\underset{\sim}{g} + \frac{1}{Re}\nabla^2\underset{\sim}{u}) \tag{6.9}$$

This equation is simplified further by the boundary-layer approximation,

$$\underset{\sim}{n}\cdot\nabla p \approx \underset{\sim}{n}\cdot\underset{\sim}{g} \tag{6.10}$$

which eliminates the coupling between the pressure boundary condition and the velocity field.†

In curvilinear coordinates, the airfoil surface is a line of constant η, and ∇η is a vector normal thereto. Thus Eq. (6.10) is equivalent to

$$\nabla\eta\cdot\nabla p = \underset{\sim}{g}\cdot\nabla\eta \tag{6.11}$$

Using the chain rule to expand ∇η and ∇p, Eq. (6.11) becomes

$$(\xi_x\eta_x + \xi_y\eta_y)p_\xi + (\eta_x^2 + \eta_y^2)p_\eta = \eta_x g_1 + \eta_y g_2 \tag{6.12}$$

where g_1 and g_2 are the x- and y-components of $\underset{\sim}{g}$.

Equation (6.12) constitutes a Neumann boundary condition for the pressure on the body surface. In order for the line-SOR calculation of the pressure to converge, Eq. (6.12) must be incorporated into the difference equation (5.19) evaluated either on the body or one line off the body. As Roache [11] emphatically points out, it is insufficient simply to extrapolate the body values from the field without first modifying the coefficients in Eq. (5.19), subject to Eq. (6.12). The most straightforward approach, eliminating the need for extrapolation altogether, is to evaluate and solve the pressure equation on the body simultaneously with that in the field.

---

† All attempts to use Eq. (6.9) as the pressure boundary condition led to divergent pressure solutions, apparently because the pressure and velocity calculations are not done simultaneously.

Letting the η-line for $j=s$ represent the airfoil surface, and using central-difference approximations (Appendix A) for p_ξ and p_η in Eq. (6.12), the following expression is obtained for $p_{i,s-1}$:

$$\begin{aligned} p_{i,s-1} = p_{i,s+1} &+ \frac{(\xi_x\eta_x + \xi_y\eta_y)}{(\eta_x^2 + \eta_y^2)}(p_{i+1,s} - p_{i-1,s}) \\ &- \frac{2(\eta_x g_1 + \eta_y g_2)}{\eta_x^2 + \eta_y^2} \end{aligned} \tag{6.13}$$

Using first-order one-sided difference approximations (Appendix A) for the η-derivatives in Eq. (5.5), and combining the result with Eq. (6.13), the difference equation for the pressure on the body reduces to

$$\begin{aligned} &\hat{A}_{i,s}\, p^{n+1}_{i-1,s} + \hat{B}_{i,s}\, p^{n+1}_{i,s} + \hat{C}_{i,s}\, p^{n+1}_{i+1,s} \\ &+ \hat{E}_{i,s}\, p^{n+1}_{i,s+1} + \hat{G}_{i,s}\, p^{n+1}_{i+1,s+1} + \hat{H}_{i,s}\, p^{n+1}_{i-1,s+1} = F_{i,s} \end{aligned} \tag{6.14}$$

where

$$\begin{aligned} \hat{A}_{i,s} = &\frac{1}{4}(3\hat{W}_{i-1,s} + \hat{W}_{i+1,s}) + \frac{1}{2}(\hat{X}_{i-1,s} + \hat{X}_{i,s}) \\ &- \frac{(\xi_x\eta_x + \xi_y\eta_y)}{2(\eta_x^2 + \eta_y^2)}(\hat{Z}_{i,s} + \hat{Z}_{i,s+1}) \end{aligned} \tag{6.15}$$

$$\hat{B}_{i,s} = -(\hat{W}_{i+1,s} + \hat{W}_{i-1,s} + 2\hat{Z}_{i,s+1}) \tag{6.16}$$

$$\begin{aligned} \hat{C}_{i,s} = &\frac{1}{4}(3\hat{W}_{i+1,s} + \hat{W}_{i-1,s}) - \frac{1}{2}(\hat{X}_{i+1,s} + \hat{X}_{i,s}) \\ &+ \frac{(\xi_x\eta_x + \xi_y\eta_y)}{2(\eta_x^2 + \eta_y^2)}(\hat{Z}_{i,s} + \hat{Z}_{i,s+1}) \end{aligned} \tag{6.17}$$

$$\hat{E}_{i,s} = 2\hat{Z}_{i,s+1} \tag{6.18}$$

$$\hat{G}_{i,s} = \frac{1}{2}(\hat{X}_{i+1,s} + \hat{X}_{i,s+1}) \tag{6.19}$$

$$\hat{H}_{i,s} = -\frac{1}{2}(\hat{X}_{i-1,s} + \hat{X}_{i,s+1}) \tag{6.20}$$

and

$$F_{i,s} = \frac{(\eta_x g_1 + \eta_y g_2)}{(\eta_x^2 + \eta_y^2)}(\hat{Z}_{i,s} + \hat{Z}_{i,s+1}) \tag{6.21}$$

Note that δ_t has been set equal to zero on the body.

6.5. Re-entrant Boundaries

Re-entrant boundaries occur wherever a branch cut is made in the physical plane (Figure 1). Velocity and pressure and gradients thereof must be continuous across these boundaries, so the re-entrant boundary conditions are periodic in the transformed plane. To avoid extrapolating these boundary values from the field, the physical variables on both sides of the cut are calculated simultaneously. That is, two ξ-lines that meet on the cut represent a single ξ-line as far as the solution algorithms are concerned, and the η-direction matrix inversion is continuous across the wake.

6.6. Trailing Edge

The body-fitted coordinate system shown in Figure 1 is of the C-type or wake type, in which the η-lines begin and end on the outflow boundary.† If the airfoil surface coincides with the line η=s, then the two points $\xi=\ell$ and ξ=r occur at the trailing edge, and the re-entrant segments are defined by $\xi \leq \ell$ and $\xi \geq r$ along η=s.

---

† As opposed to an O-type coordinate system, in which the η-lines are closed curves.

At the trailing edge, which is a sharp point in the physical plane, the surface-normal vector ($\nabla\eta$) is discontinuous, making the pressure boundary condition (6.11) also discontinuous. This singularity is peculiar to the C-type coordinate system rather than the flow itself, and it can be circumvented on physical grounds.

The no-slip condition implies that there can be no unbalanced force on the fluid at the trailing edge. Neglecting the viscous stress, as in section 6.4., the projection of the momentum equation in an arbitrary direction $\underset{\sim}{\tau}$ reduces to

$$\underset{\sim}{\tau}\cdot\nabla p \approx \underset{\sim}{\tau}\cdot\underset{\sim}{g} \qquad (6.22)$$

If $\underset{\sim}{\tau}$ is tangent to the re-entrant segments at $\xi=\ell$ and $\xi=r$ on $\eta=s$, then the pressure boundary condition at the trailing edge becomes

$$p_\xi = J^{-1}(\eta_y g_1 - \eta_x g_2) \qquad (6.23)$$

as $\xi\to\ell_-$ and $\xi\to r_+$.

Computationally, the following substitutions are made in the line-SOR equation (5.30) at the trailing edge.

$$p_{\ell+1,s} = p_{\ell-1,s} + \frac{2}{J}(\eta_y g_1 - \eta_x g_2) \qquad (6.24)$$

$$p_{r-1,s} = p_{r+1,s} - \frac{2}{J}(\eta_y g_1 - \eta_x g_2) \qquad (6.25)$$

CHAPTER VII

COMPUTATIONAL ADJUSTMENTS

7.1. Turbulence Model

Baldwin and Lomax [14] have formulated an algebraic turbulence model for separated flow, which is used herein to include the effects of small-scale eddies in the Reynolds-averaged Navier-Stokes equations. This model generates an eddy viscosity $\mu_T \geq 0$ such that the nondimensional physical viscosity becomes

$$\mu = 1 + \mu_T \tag{7.1}$$

and $\mu_T \to 0$ on the body and in the freestream. Transition is set at the point of minimum pressure on either side of the stagnation point, with the turbulence propagating downstream into the wake.

7.2. Artificial Viscosity

Space-centered differencing leads to algorithms that are algebraically convenient, second-order accurate, and unfortunately susceptible to instability, especially at high Reynolds number. Some form of artificial dissipation is usually needed to diffuse spurious oscillations, even with fully implicit methods. This task is accomplished herein by adding an extra viscous term to the (nondimensional) right-hand side of Eq. (2.12); specifically[†],

$$\mathrm{LHS}(2.12) = \mathrm{RHS}(2.12) + \frac{1}{\mathrm{Ra}}\frac{\partial}{\partial x_j}\left(\frac{\partial u_i}{\partial x_j} + \frac{\partial u_j}{\partial x_i}\right) \tag{7.2}$$

The additional term is the same as the viscous term in (2.12), but with

---

[†] Equation (7.2) uses the Einstein summation convention and the cartesian coordinates of Chapter II.

$\mu=1$ and Re replaced by the artificial Reynolds number [15], defined by

$$\frac{1}{Ra} = \frac{\varepsilon|\nabla\cdot\underset{\sim}{u}|}{J} \tag{7.3}$$

where $\varepsilon \geq 0$ and J is the Jacobian of the coordinate transformation, given by Eqs. (3.16) and (3.18).

Ideally, the artificial viscous term should vanish wherever the calculated flow satisfies continuity. The main advantage of (7.3), however, is that it behaves like a switched filter, turning on wherever instabilities are most likely to arise. For situations in which $\nabla\cdot\underset{\sim}{u}$ varies sharply across the field, an extended definition of Ra is

$$\frac{1}{Ra} = \left(\frac{\varepsilon|\nabla\cdot\underset{\sim}{u}|}{J}\right)_{ave} \tag{7.4}$$

where the subscript "ave" indicates a three-point average in the direction of sharp variation. In either case, the additional term in (7.2) introduces both implicit and explicit artificial viscosity into the approximate-factorization scheme discussed in Chapter IV.

7.3. Pressure Smoother

The primary source of instability in the calculated flow is the pressure equation. Regardless of the method of solution or the degree of convergence, the right-hand side of the difference equation (5.19) contains only information from the previous time step. As a result, numerical oscillations in the velocity field are fed directly into the pressure equation, worsening the situation with each time step.

Viscosity, either real or artificial, dissipates oscillations in both pressure and velocity. The need for artificial viscosity can, however, be reduced somewhat by smoothing the right-hand side of the pressure equation. Moreover, a three-point average in the direction of sharp variation improves results considerably. Specifically, Eq. (5.19) is replaced by

$$\mathrm{LHS}(5.19) = \frac{1}{4}(F_{i+1,j} + 2F_{ij} + F_{i-1,j}) \tag{7.5}$$

which is more or less equivalent to the addition of a term proportional to $\nabla^4 p$ in the pressure equation.

CHAPTER VIII

COMPUTATIONAL RESULTS

8.1. Coordinate System for NACA 66_3018 Airfoil

Thompson [15] has generated a body-fitted curvilinear coordinate system for the NACA 66_3018 airfoil, based on an assumed Reynolds number of 100,000. This coordinate system, shown in Figure 2, is suitable for calculations at Reynolds numbers within an order of magnitude or so of 100,000. If $Re \gg 100{,}000$, the flow resolution in the viscous region will be poor, because the mesh spacing is not fine enough next to the body. On the other hand, if $Re \ll 100{,}000$, round-off problems may arise because the mesh spacing is too fine. The transformed plane is a 113 x 51 rectangular grid with unit mesh spacing.

8.2. Computational Parameters

In all the calculations reported below, the time step is fixed at $\Delta t=0.01$. The gradual start consists of 100 time steps of uniform acceleration, with the x and y body-force components given respectively by

$$g_1 = \cos \alpha$$

$$g_2 = \sin \alpha$$

After the first 100 time steps, at $t=1.00$, the calculation is stopped and then restarted with the initial condition $\Delta u = \Delta v = 0$. Since a three-point backward time difference is used in the AF momentum solver (section 4.2.), the restart is necessary to avoid overshooting the values of Δu and Δv at $t=1.01$. Had a nonlinear (e.g., cosine) acceleration been used, the stop and restart would be unnecessary, because the body force would be a continuous function of time. As it is, the body force for the linear start is a step function, discontinuous at t=0.0 and t=1.0.

The number of iterations in the line-SOR pressure solver is fixed at thirty per time step, with the acceleration parameter set at ω=1.85. Thirty iterations are probably more than necessary, although stability does improve slightly with the iteration count. Reducing the number to twenty degrades stability and convergence only slightly; further reduction to ten or fewer seems to promote instability, due to poor convergence. The ω-value of 1.85 is not necessarily optimal, but rather the result of some experimentation. Values from 1.8 to 0.0 lead to increasingly slower convergence, while the optimum seems to lie somewhere between 1.8 and 1.9.

The artificial viscosity coefficient can be set at any value $\varepsilon \geq 0$, depending on how stable the undamped calculated flow is. Since this parameter alters the local Reynolds number (section 7.2.), it is desirable to keep the value of ε as low as possible. The pressure smoother (section 7.3.) is used in all calculations, since it does not add any fictitious terms directly to the momentum equation, nor does it affect the spatial truncation error.

8.3. Results for Re = 1000 and α = 6°

Even though the coordinate system (Figure 2) was designed for Re = 100,000, it is worthwhile to make a calculation at low Reynolds number, without including the turbulence model and the artificial viscosity. The object here is to examine the qualitative behavior of the predicted flow field in the absence of artificial stabilizing mechanisms.

The results presented in Figures 3 - 12 were obtained for the conditions

$$\alpha = 6^\circ$$

$$Re = 1000$$

$$\epsilon = 0$$

$$\mu_T = 0$$

Figures 3 – 6 show sequentially the evolution of the pressure distribution along the airfoil.† Downstream of the leading edge, the pressure on the lower (windward) surface gradually falls, while the pressure on the upper surface gradually rises. At $t=3.0$ the two distributions have begun to overlap, with the point of intersection moving upstream to $x \sim 0.5$ by $t=4.0$.

Figures 7 – 12 illustrate the development of the velocity field between $t=2.0$ and $t=4.0$. Around the leading edge (Figures 7 and 8), there is hardly any change in the velocity profiles. Moreover, examination of the entire flow field (Figures 9 and 10) reveals little change except near the trailing edge (Figures 11 and 12). Here, a vortex just beginning to form at $t=2.0$ has grown considerably by $t=4.0$.

The calculation was terminated at $t=4.3$, due to instability associated with the trailing-edge vortex. A restart could have been initiated at $t=4.0$, with artificial viscosity added for stabilization, but this seemed unwarranted. The information generated for $t \leq 4.0$ gives an adequate picture of the flow at low Reynolds number; and the instability is probably due to the mesh spacing, which is much too fine.

---

† The leading edge coincides with $x=0$, and the trailing edge with $x=1$. The pressure coefficient C_p is defined by $C_p = \dfrac{p - p_\infty}{\frac{1}{2}\rho U_\infty^2}$.

8.4. Results for Re = 40,000 and α = 0

Mueller [16] has conducted wind-tunnel tests of the NACA 66_3018 airfoil at Reynolds numbers from 40,000 to 400,000. In order to evaluate the applicability of the combined AF/SOR scheme for real flow problems, calculations have been made for comparison with Mueller's data. The computational results presented in Figures 13 - 34 were obtained for the conditions

$$\begin{aligned} Re &= 40{,}000 \\ \varepsilon &= 1\ ,\ t \leq 1.0 \\ \varepsilon &= 10,\ t > 1.0 \\ \alpha &= 0^\circ \text{ and } 6^\circ \end{aligned}$$

Trial calculations with $\varepsilon=0$ became unstable around the leading edge at $t\approx0.8$. With $\varepsilon=1$, stability problems developed in the wake, near the trailing edge, at $t\approx1.8$. Thus, to maintain stability for Re = 40,000, it is necessary to increase the artificial viscosity coefficient from 1 to 10 when $t>1$. Furthermore, to keep the flow well-behaved in the wake, it is advisable to activate the turbulence model prior to $t=3.0$.†

The computation for $\alpha=0$ (Figures 13 - 23) was executed from $t=0.0$ to $t=2.0$ with $\mu_T = 0$. The turbulence model was activated at $t=2.01$, and execution continued until $t=5.0$ (a total of 500 time steps). The combined eddy/artificial viscosity kept the flow orderly, and no

---

† Since the turbulence model increases the local viscosity, it has a stabilizing effect on the flow, especially in the wake. As a result, the turbulence helps to suppress the development of unstable trailing-edge vortices of the kind discussed in section 8.2. (Figure 12).

instabilities were apparent when the calculation was finally stopped.

Figures 13 - 17 indicate the change in the pressure distribution between t=1.0 and t=5.0. The calculated variation of C_p is symmetric along the airfoil (as it should be), and the pressure drop at t=3.0, between x=0.8 and x=1.0, is precipitated by vortices at the trailing edge (Figure 22). These vortices have begun to damp out by t=5.0.

The agreement between the computed C_p and the wind-tunnel data is good everywhere except near the leading and trailing edges. Further calculation would probably eliminate the discrepancy at the trailing edge, since the computed pressure seems to be falling there with time. The leading-edge problem may be the indirect result of continuity violations and artificial viscosity, via Eq. (7.4) ,[†] and might or might not be corrected by additional computation.

Figures 18 - 23 show the change in the velocity field between t=2.0 and t=5.0. For the most part, the viscous layer around the body is unrealistically thick, with separation occurring at center chord (Figure 19). This is unavoidable with the AF/SOR method in its present form, since it is caused by the artificial viscosity, which is necessary for stability at high Reynolds number.

At t=2.0 the leading-edge velocity profiles (Figure 20) are well-behaved, though getting thicker in the x-direction. By t=5.0., the profile shapes (Figure 21) have begun to alternate somewhat, due to the variation of the artificial viscosity along the body. This

---

[†] Experimentation with the AF/SOR method has indicated that the greater the penetration (continuity violation) around the leading edge, the gentler the pressure gradient there.

alternation could be the harbinger of trouble for $t > 5.0$, but the velocity and pressure distributions are still symmetric and quite stable at $t = 5.0$.

8.5. Results for Re = 40,000 and α = 6°

The computation for $\alpha = 6°$ (Figures 24 - 34) was executed from $t = 0.0$ until $t = 5.0$, with the turbulence model activated in the second time step ($t = 0.02$). No instabilities were encountered, nor were any apparent when the calculation was terminated.

The evolution of the pressure distribution along the body (Figures 24 - 28) is qualitatively the same as for Re = 1000. In this case, however, the slopes are steeper, and the overlap for the upper and lower surfaces takes longer to develop. Comparison with the wind-tunnel data in Figure 28 shows the computed curves to be mysteriously displaced from the experimental curves, but with the same general shape, including the double overlap. Moreover, in Figures 28 and 17 alike, the calculated pressure distributions appear to be right-shifted from the experimental results. In the 6-degree case, the shift may be due to poor resolution of the calculated minimum pressure on the upper surface near the leading edge.

Examination of the velocity field (Figures 29 and 30) reveals substantial change between $t = 2.0$ and $t = 5.0$. The upper- and lower-surface separation points, located respectively at $x \approx 0.6$ and $x \approx 0.8$ when $t = 2.0$, have moved upstream to $x \approx 0.3$ and $x \approx 0.7$ by $t = 5.0$. The leading-edge velocity profiles exhibit a gradual thickening (Figures 31 and 32), and vortices have developed at the trailing edge by $t = 5.0$ (Figures 33 and 34). As in the calculation for $\alpha = 0$, the viscous layer is much too thick around the body.

8.6. Other Calculations

Prior to making the calculations for the 66_3018 airfoil, a great deal of personal effort and computer time was invested in calculations for the NACA 64A010 airfoil at Re = 2,000,000, using a coordinate system generated by Cooper [8]. In fact, most of the developmental work for the AF/SOR scheme was done with the 64A010 airfoil.† To maintain stability with this coordinate system and Reynolds number, however, the required values of ε were 10 during the gradual start and 100 thereafter. In other words, the amount of artificial viscosity needed for Re = 2,000,000 was an order of magnitude greater than that for 40,000, making the viscous region about three times thicker at the higher Reynolds number.

The stability problem is probably related to the coordinate geometry, specifically to the mesh spacing. Equation (3.11) determines the η-line spacing next to the body; so if Re increases by two orders of magnitude, the spacing decreases by one order of magnitude. It is common knowledge that, for explicit methods, the maximum stable time step decreases with the minimum finite-difference cell dimension. The same

---

† The AF/SOR method, as it now stands, represents the last of three attempts to construct an approximate-factorization algorithm for incompressible flow. The first two versions, while invaluable from an experiential standpoint, produced little in the way of communicable results.

is apparently true for implicit/explicit methods such as AF/SOR, but the relationship is more difficult to quantify. In either case, it seems that <u>more</u> viscosity may be needed for stability when the mesh spacing is reduced with the time step and Reynolds number fixed. Additional calculations are needed to verify this for AF/SOR.

CHAPTER IX
CONCLUSION

9.1. Discussion

The combined AF/SOR algorithm is implicit in its solution of the momentum equation, but explicit in the sense that the pressure/continuity solution is lagged in time. As a result, the method is far less stable than the compressible-flow AF scheme of Beam and Warming. For a time step $\Delta t = 0.01$, the maximum practical Reynolds number is probably around Re = 10,000, if the artificial viscosity is to be kept tolerably low ($\varepsilon \leq 1$). Furthermore, since stability may depend on mesh spacing as well as viscosity, the body-fitted coordinate system should be generated for the Reynolds number in question or for a lower value, but not a higher. Increasing the Re-value in the coordinate generation (section 3.1.) reduces the mesh spacing. This, in turn, demands more artificial viscosity for stability, which contaminates the numerical results. Since truncation error is preferable to instability, it seems advisable to keep the mesh a little on the coarse side.

By way of comparison with conventional implicit methods, point-SOR calculations can be stabilized at $Re \simeq 10^6$ with $\varepsilon = 1$ and $\Delta t = 0.01$. Thus, at high Reynolds number, point SOR (or some other fully implicit method) is required for incompressible flow calculations. On the other hand, at low Reynolds number ($Re < 10^4$) AF/SOR seems preferable, being passably stable and faster than point SOR by at least a factor of two.†

Compared with compressible-flow AF calculations, AF/SOR fairs poorly. Cooper [8] reports a machine-time expenditure of 4.5 seconds per time step on the CDC Cyber 203, using the method of Beam and Warming at a freestream Mach number of 0.8 and a Reynolds number of two million. The AF/SOR calculations discussed in Chapter VIII averaged 5.5 seconds per time step on the same computer. While program optimization could markedly reduce both of these cost figures, the point is that the compressible-flow algorithm seems to require no more computer time than the incompressible solution.

In summary, the combination of approximate factorization and line SOR appears to be suitable only for incompressible flow calculations at low Reynolds number ($Re < 10^4$), when used alone. On the positive side, however, AF/SOR might serve as an initial-guess generator for iterative methods such as point SOR. It is possible that the latter approach, employed in each time step, would produce stable high-Reynolds-number solutions in relatively few iterations compared to point SOR alone.

---

† Thirty iterations of line SOR is roughly equivalent to fifty iterations of point SOR, for a single equation. Ten iterations of the line-SOR pressure solver takes roughly the same number of operations as the AF momentum solver. The net result is that AF/SOR, as used herein, requires between two and three times less work than a 50-iteration point-SOR solution for u, v, and p.

9.2. Epilogue

The results presented in Chapter VIII are in some ways disappointing, but not really surprising. While fully explicit and fully implicit methods usually have definable (or at least estimable) limits of stability, mixed methods can only be evaluated by computational experimentation. At the outset, one hopes for the best, but in the end must accept those limitations dictated by the Machine.

Incompressible flow at high Reynolds number remains a knotty problem, requiring expensive, and sometimes questionable, methods of solution. At low Reynolds number, AF/SOR offers a means of calculation that is relatively efficient. Unfortunately, most engineering problems involve high Reynolds number, whether they be aerodynamic or hydrodynamic. Only rarely are calculations needed for molasses or for concentrated shampoo.

What is needed is a method that calculates pressure and velocity simultaneously, but with the same efficiency as approximate factorization. A vectorized ADI or SOR scheme[†] could meet the simultaneity criterion but would be inefficient, requiring far more than one iteration per time step for convergence. Perhaps a clever formulation or manipulation of the pressure/continuity equation would allow factorization in the same fashion as compressible flow. Except for the method of Steger

---

[†] That is, an algorithm that inverts a 3 x 3 matrix at each point in the field to obtain the vector (u,v,p). This takes about four times as many operations as the more commonly used approach, which is to calculate u, v, and p in sequence at each point. The latter method, in effect, inverts three 1 x 1 matrices.

and Kutler [9], which converges only for the steady state, efforts in that direction have failed to produce a stable algorithm. Nevertheless, the problem is so intriguing, so deceptively simple at a glance, that it can become an obsession. Every day one thinks anew, there must be a way.

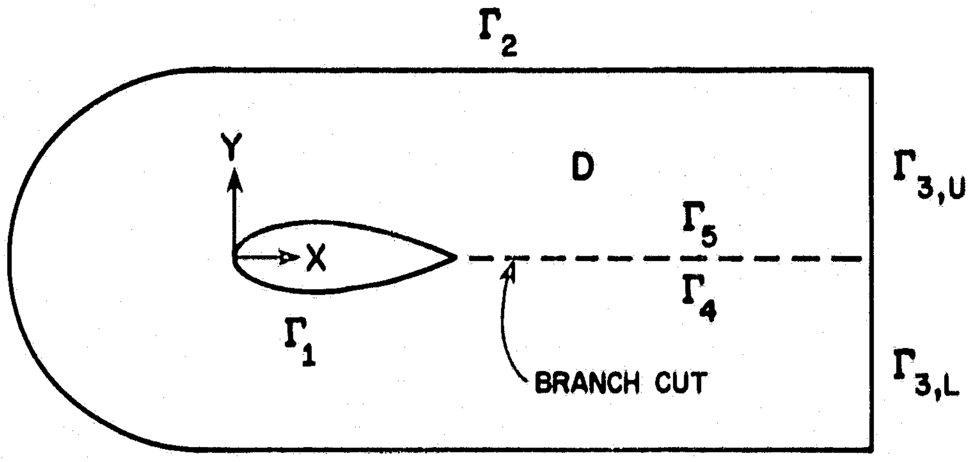

a. Physical Plane

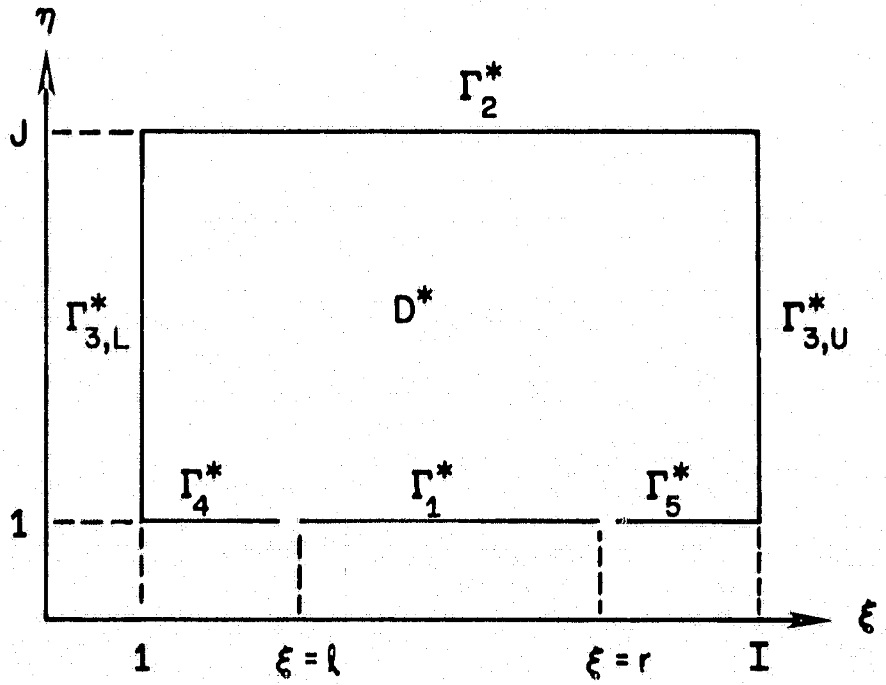

b. Transformed Plane

Figure 1. C-Type Coordinate System

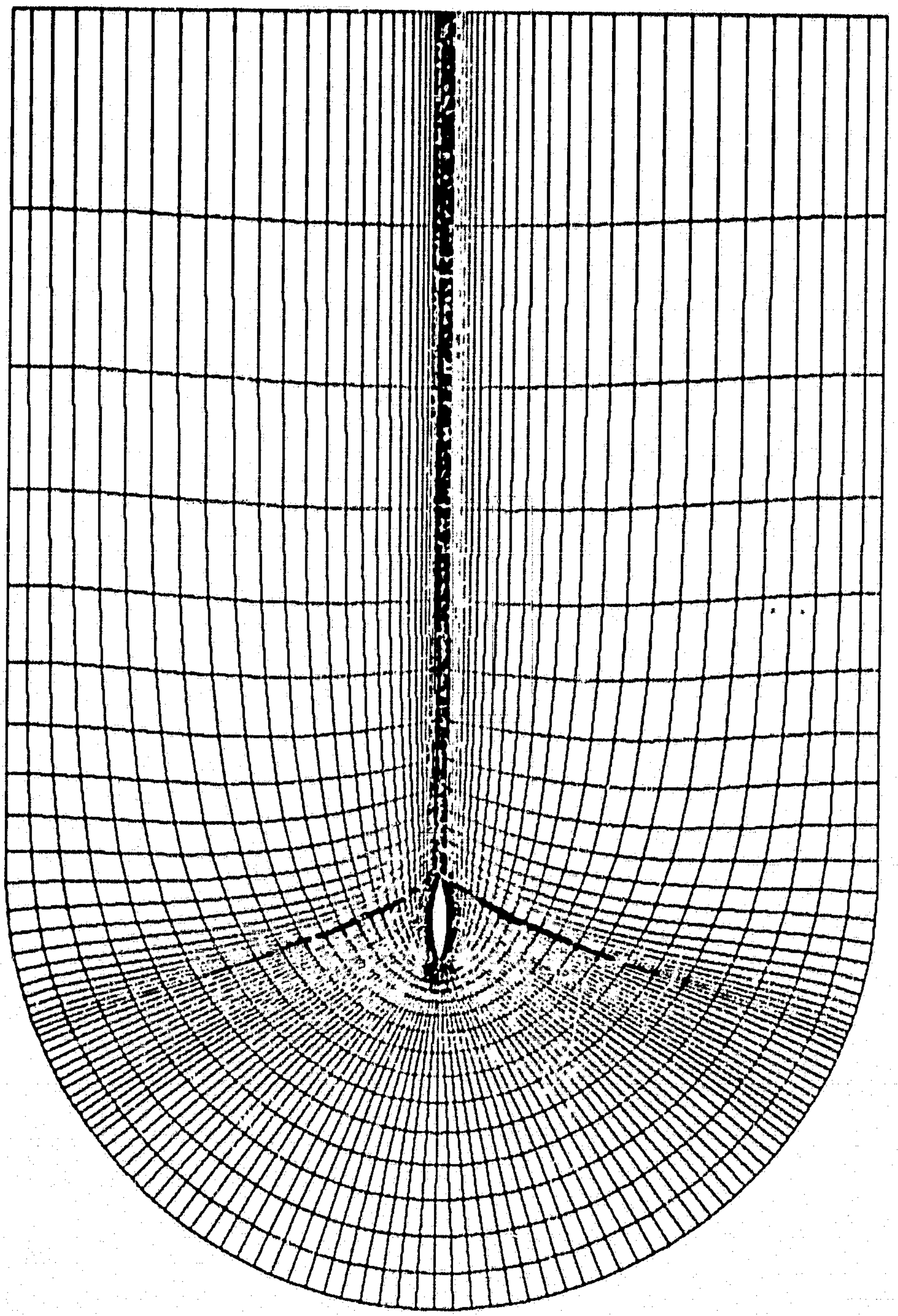

Figure 2. Coordinate System for NACA 66_3018 Airfoil

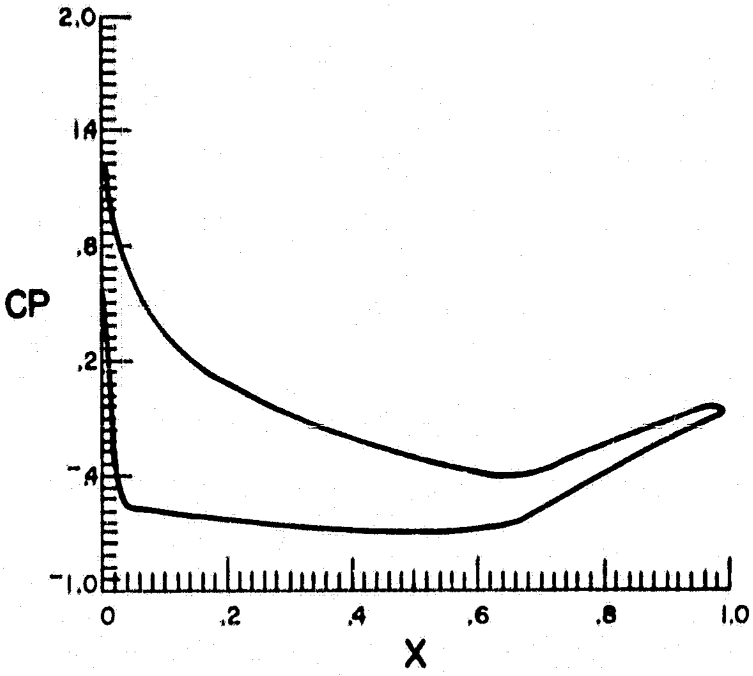

Figure 3. Pressure Distribution - Re = 1000, α = 6°, t = 1.0

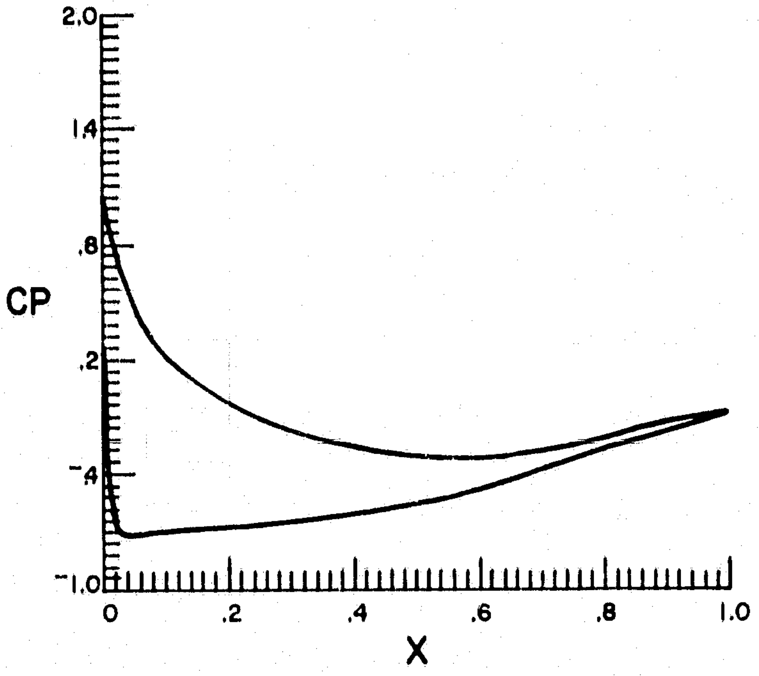

Figure 4. Pressure Distribution - Re = 1000, α = 6°, t = 2.0

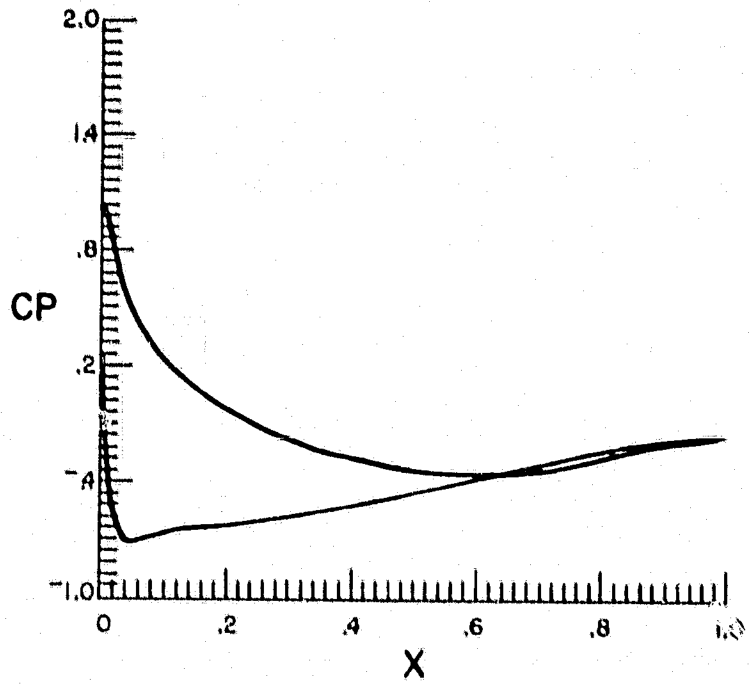

Figure 5. Pressure Distribution - Re = 1000, α = 6°, t = 3.0

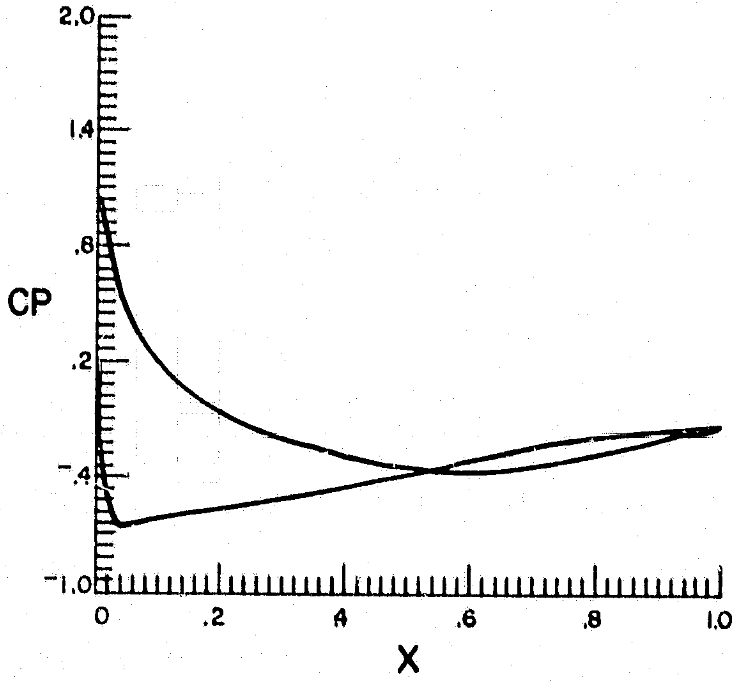

Figure 6. Pressure Distribution - Re = 1000, α = 6°, t = 4.0

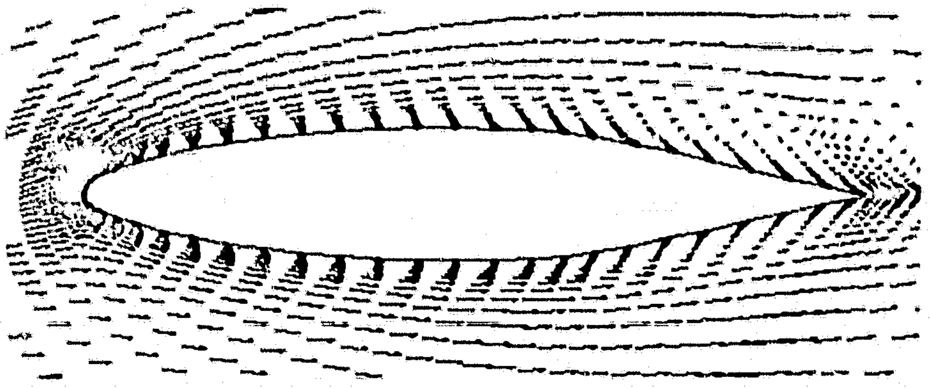

Figure 7. Velocity Field - Re = 1000, α = 6°, t = 2.0

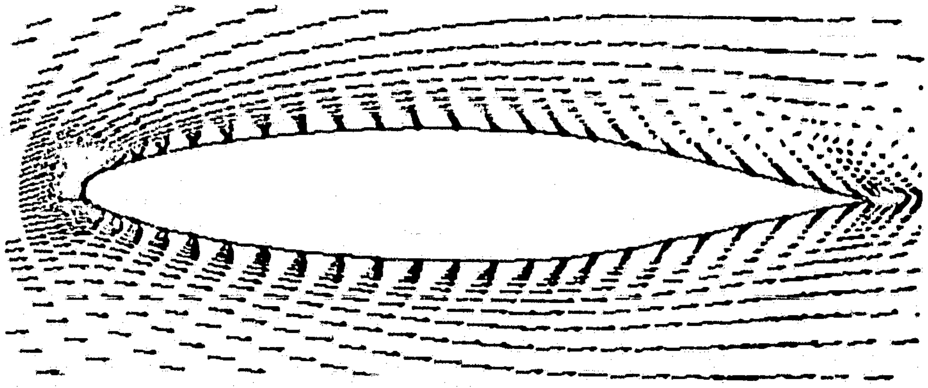

Figure 8. Velocity Field - Re = 1000, α = 6°, t = 4.0

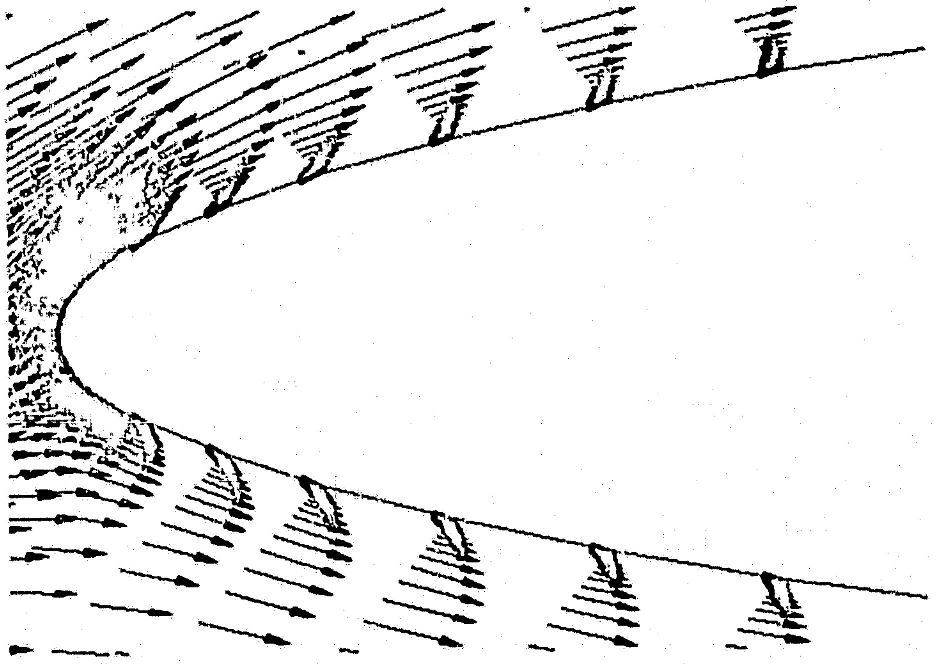

ORIGINAL PAGE IS
OF POOR QUALITY

Figure 9. Leading-Edge Velocity Profiles - Re = 1000, α = 6°, t = 2.0

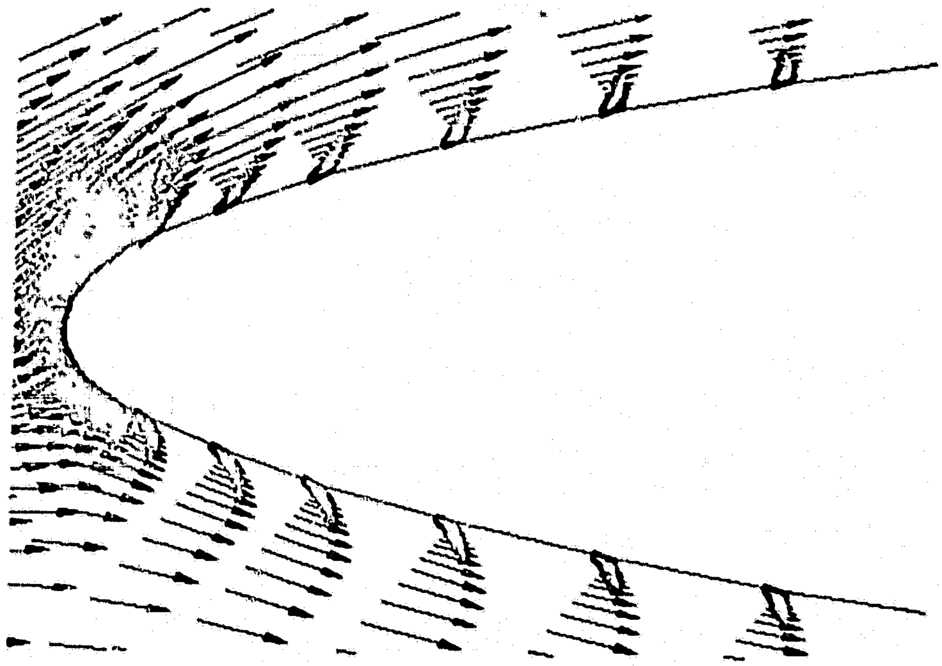

Figure 10. Leading-Edge Velocity Profiles - Re = 1000, $\alpha = 6°$, $t = 4.0$

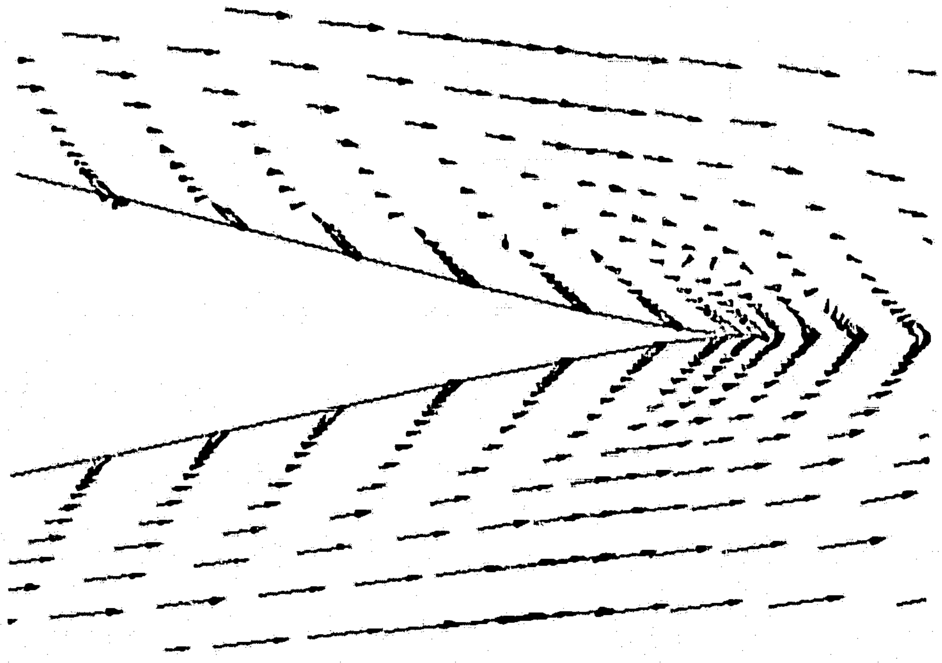

Figure 11. Trailing-Edge Velocity Profiles - Re = 1000, α = 6°, t = 2.0

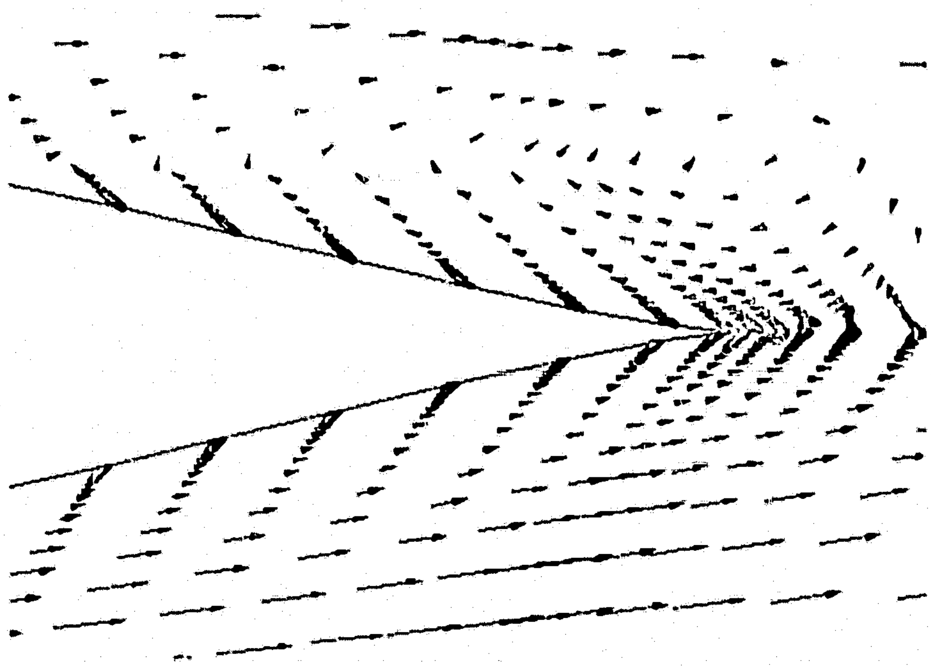

Figure 12. Trailing-Edge Velocity Profiles - Re = 1000, α = 6°, t = 4.0

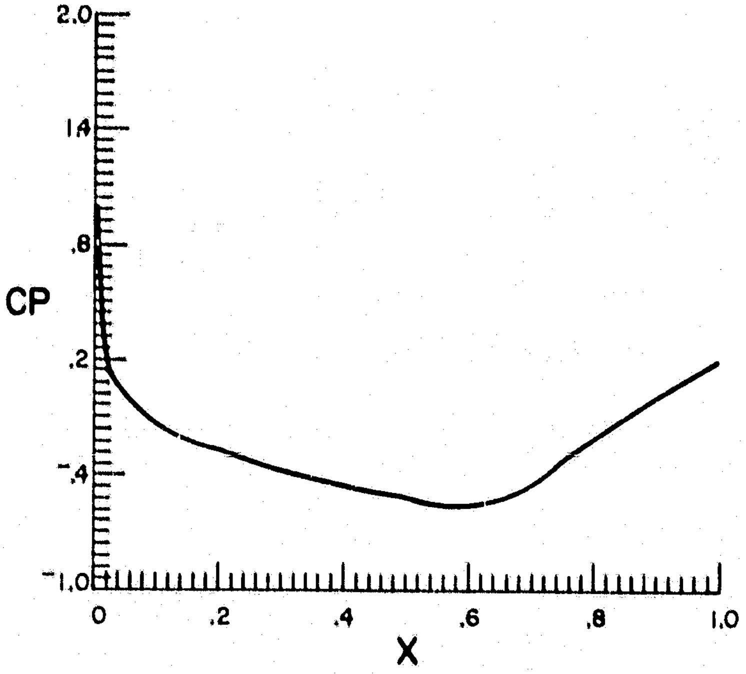

Figure 13. Pressure Distribution - Re = 40,000, α = 0°, t = 1.0

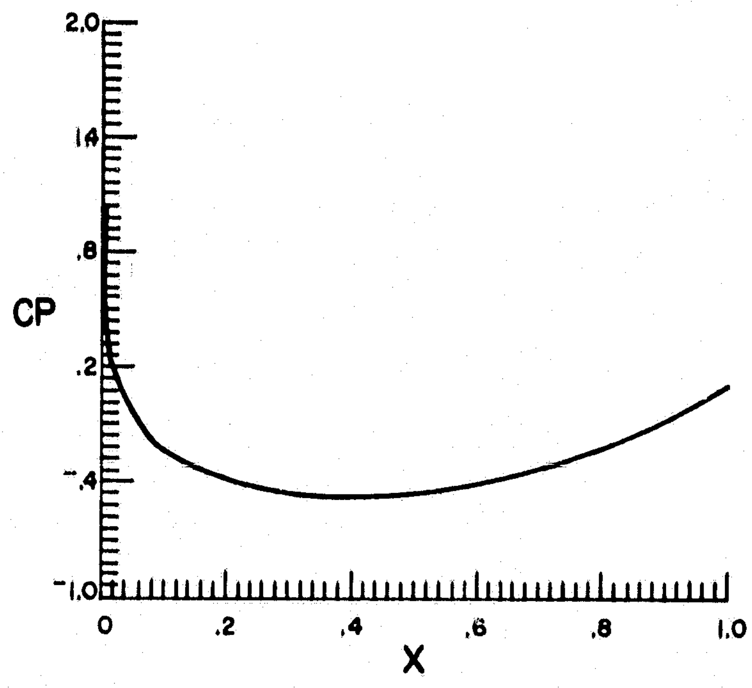

Figure 14. Pressure Distribution - Re = 40,000, α = 0°, t = 2.0

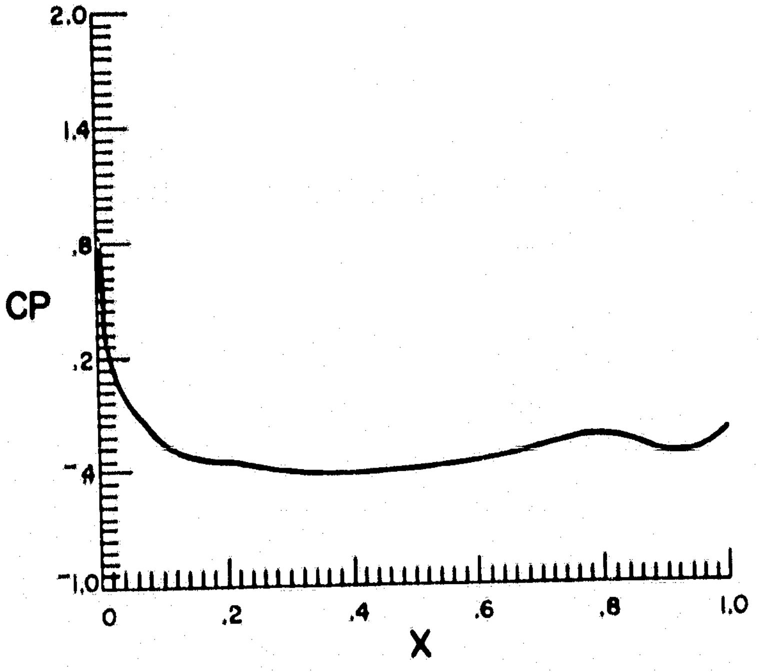

Figure 15. Pressure Distribution - Re = 40,000, α - 0°, t = 3.0

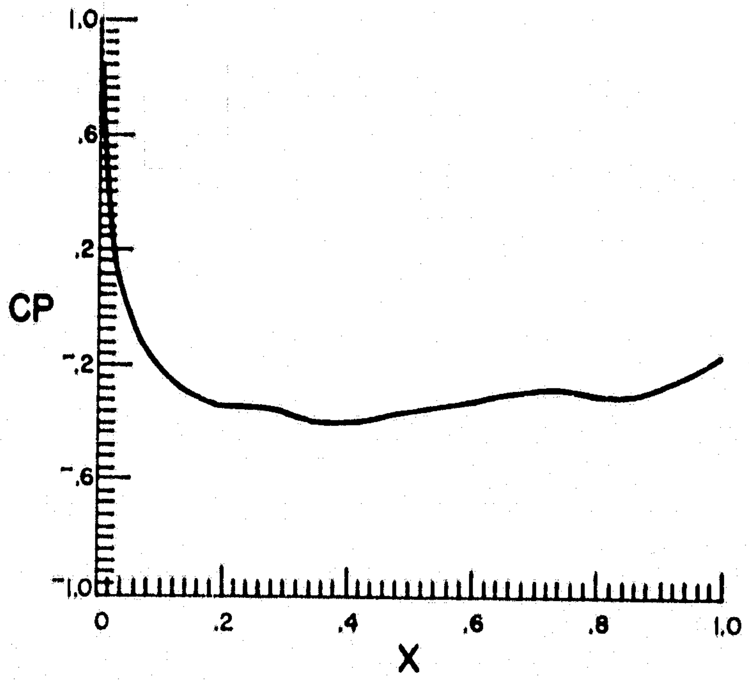

Figure 16. Pressure Distribution - Re = 40,000, α = 0°, t = 4.0

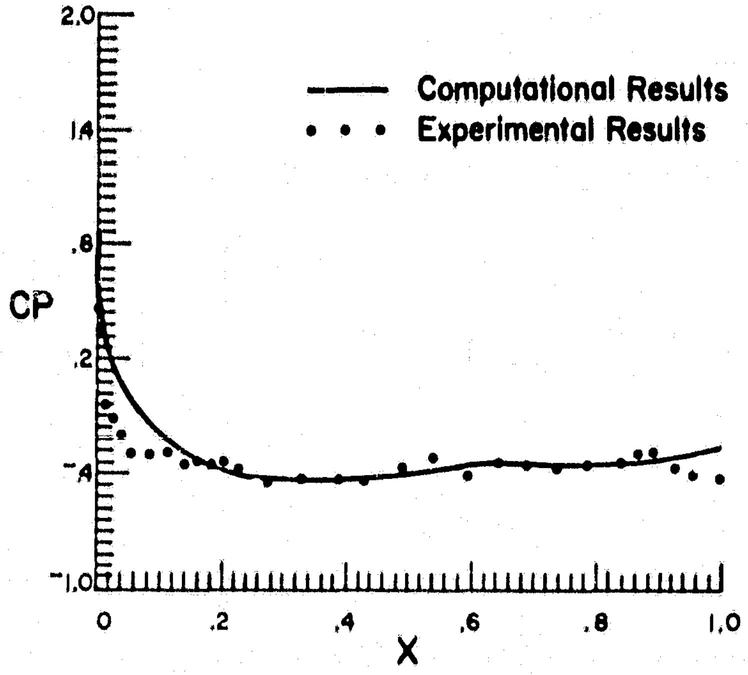

Figure 17. Pressure Distribution - Re = 40,000, α = 0°, t = 5.0

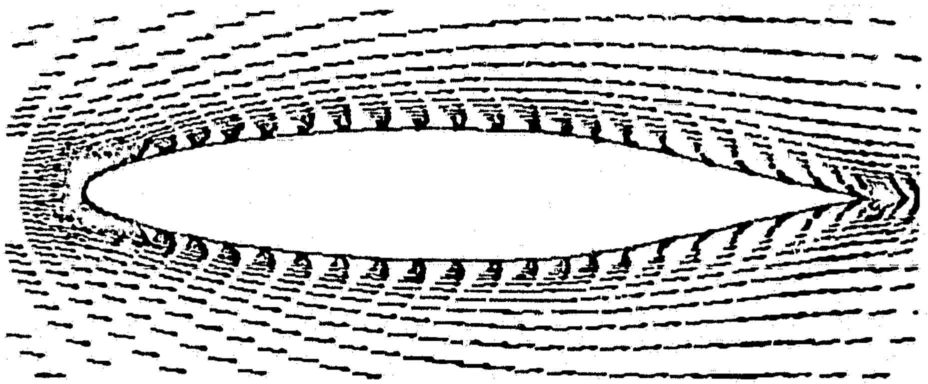

Figure 18. Velocity Field - Re = 40,000, $\alpha = 0°$, t = 2.0

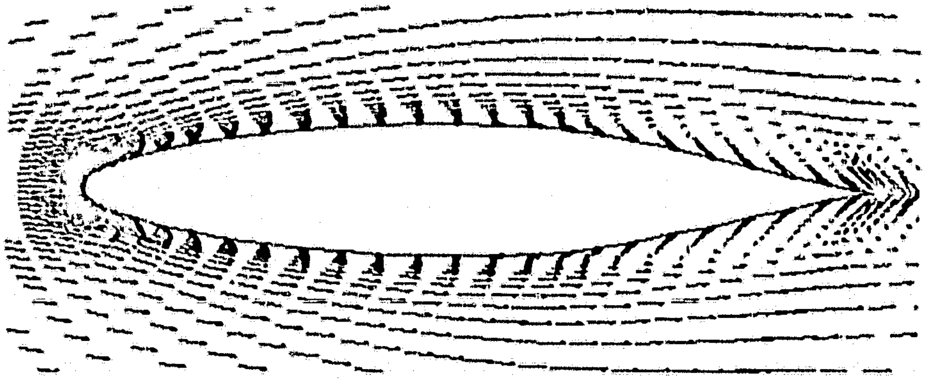

Figure 19. Velocity Field - Re = 40,000, $\alpha = 0°$, t = 5.0

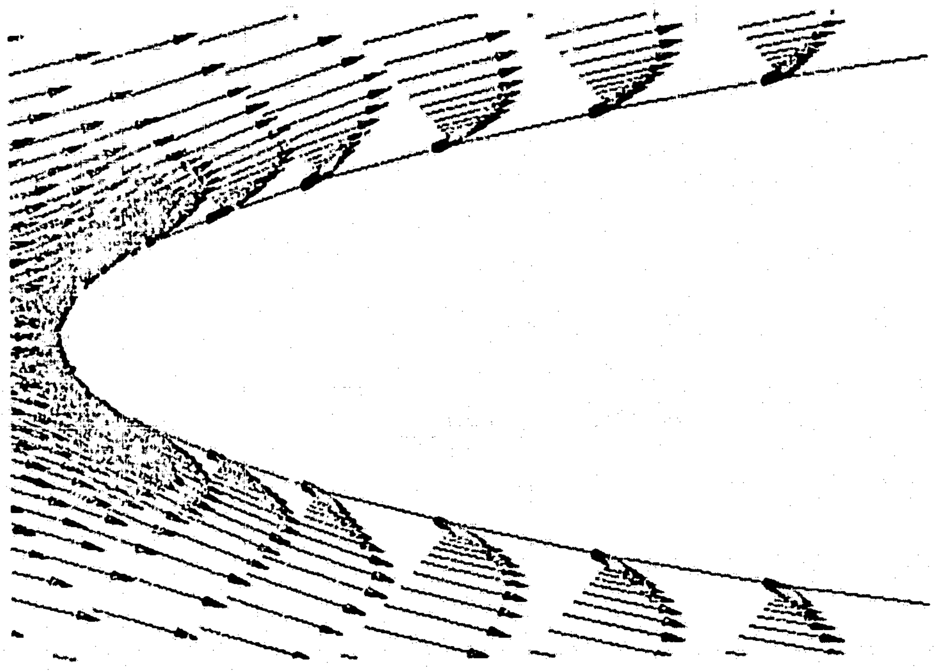

Figure 20. Leading-Edge Velocity Profiles - Re = 40,000, $\alpha = 0°$, t = 2.0

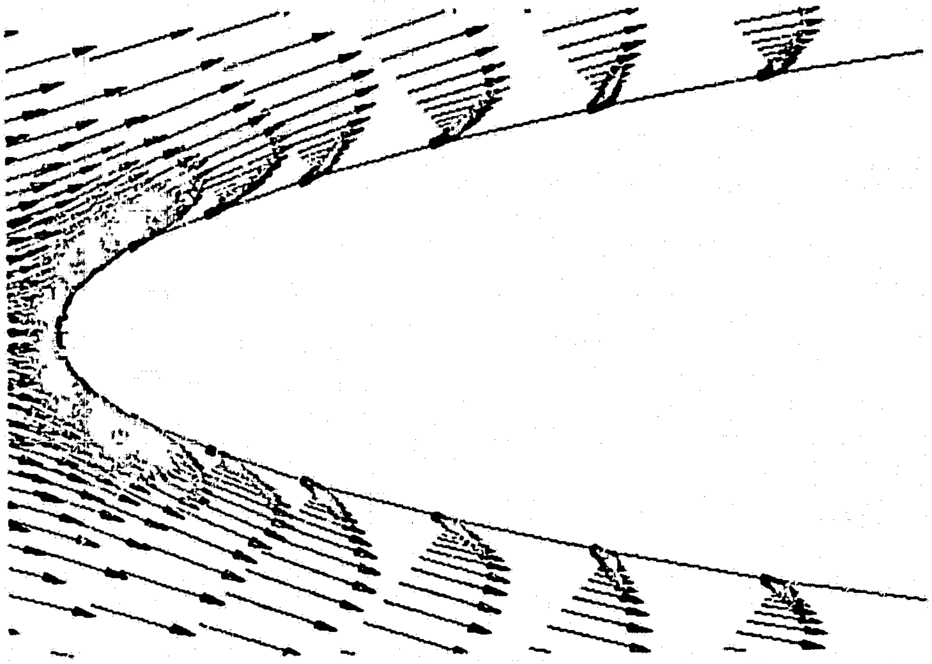

ORIGINAL PAGE IS
OF POOR QUALITY

Figure 21. Leading-Edge Velocity Profiles - Re = 40,000, $\alpha = 0°$, t = 5.0

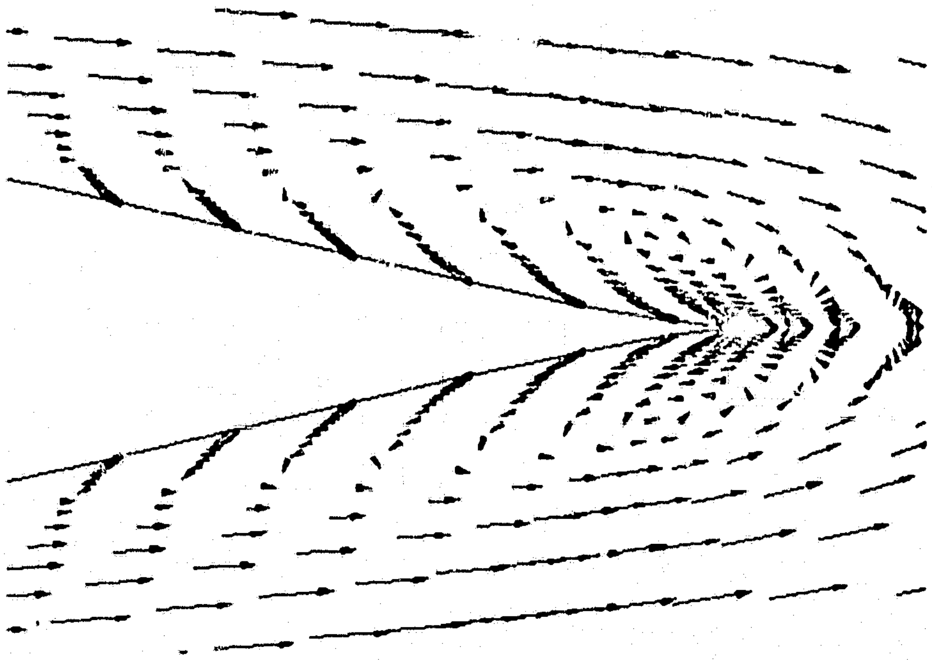

Figure 22. Trailing-Edge Velocity Profiles - Re = 40,000, α = 0°, t = 3.0

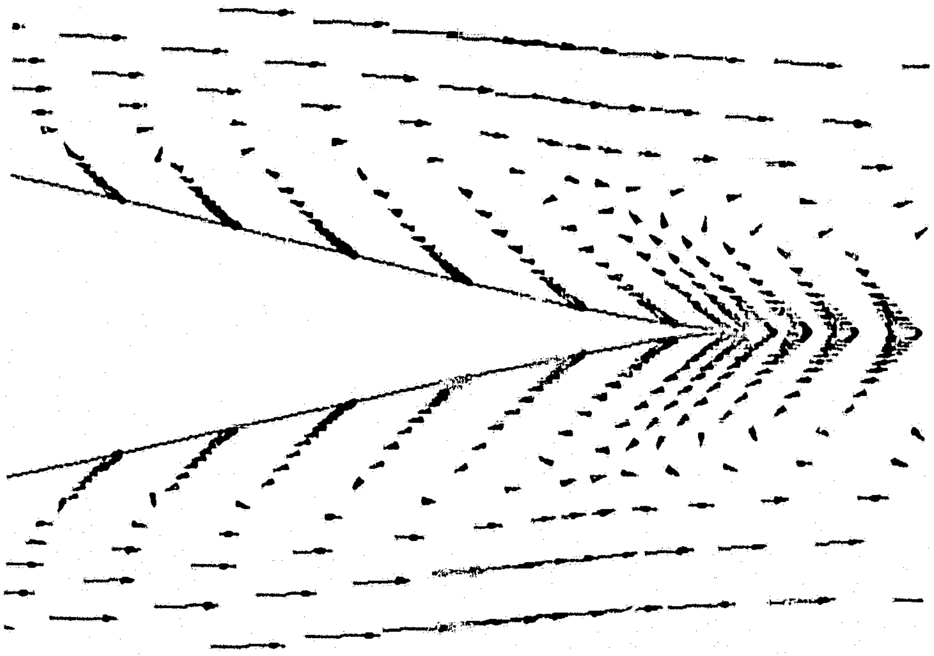

Figure 23. Trailing-Edge Velocity Profiles - Re = 40,000, α = 0°, t = 5.0

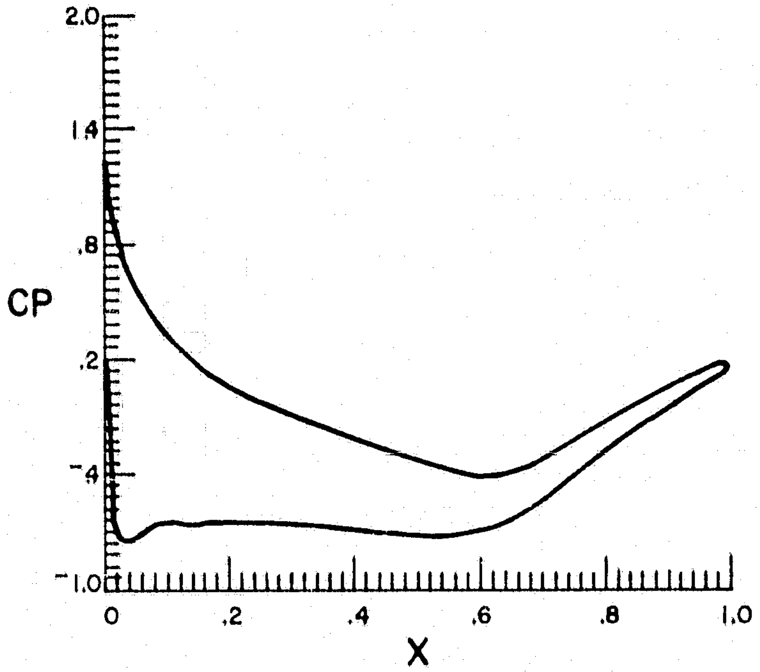

Figure 24. Pressure Distribution - Re = 40,000, α = 6°, t = 1.0

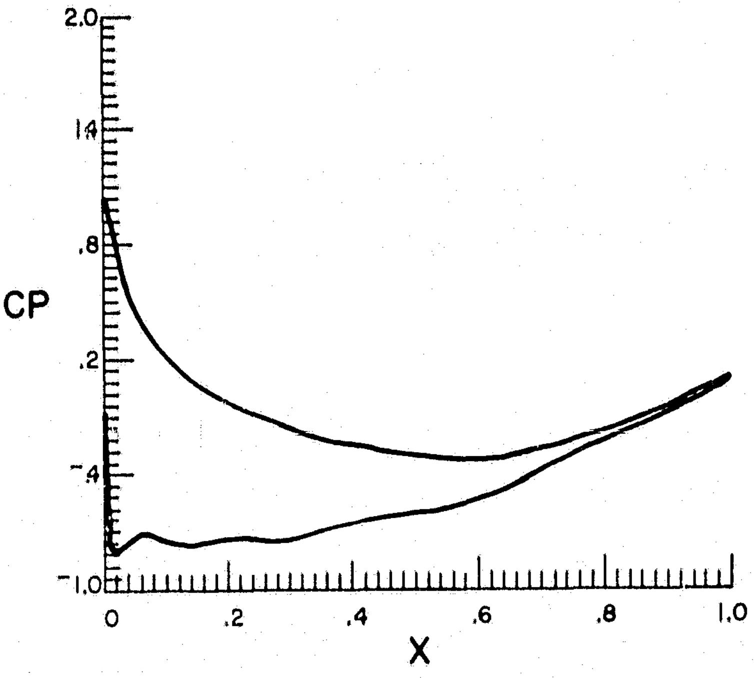

Figure 25. Pressure Distribution - Re = 40,000, α = 6°, t = 2.0

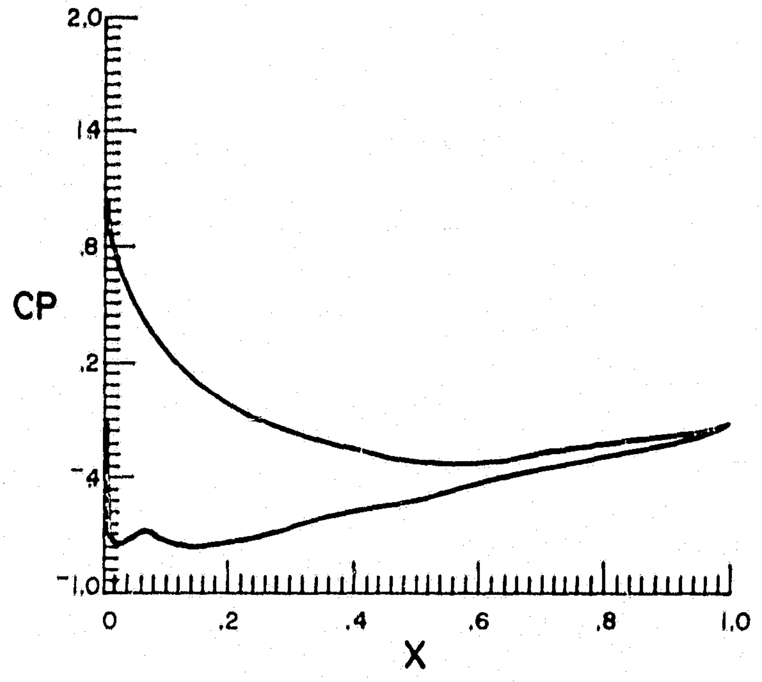

Figure 26. Pressure Distribution - Re = 40,000, α = 6°, t = 3.0

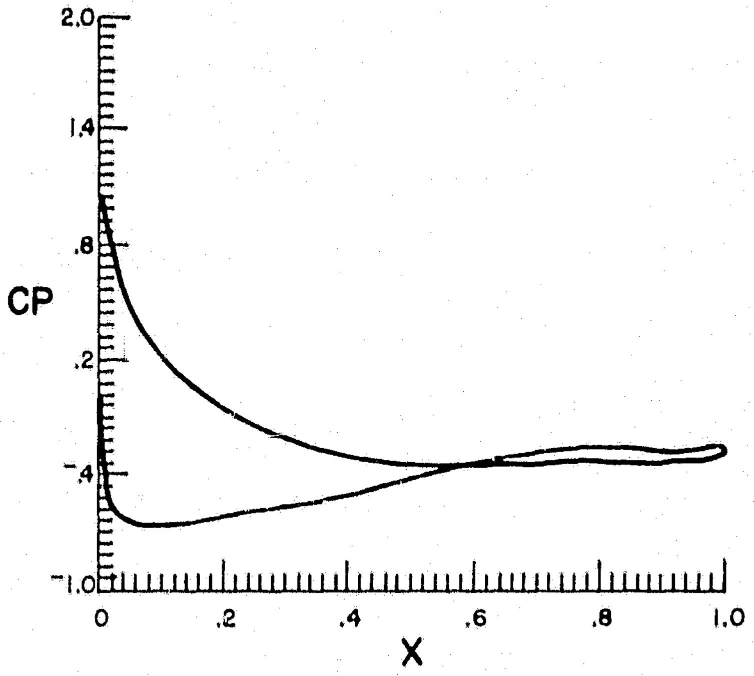

Figure 27. Pressure Distribution - Re = 40,000, α = 6°, t = 4.0

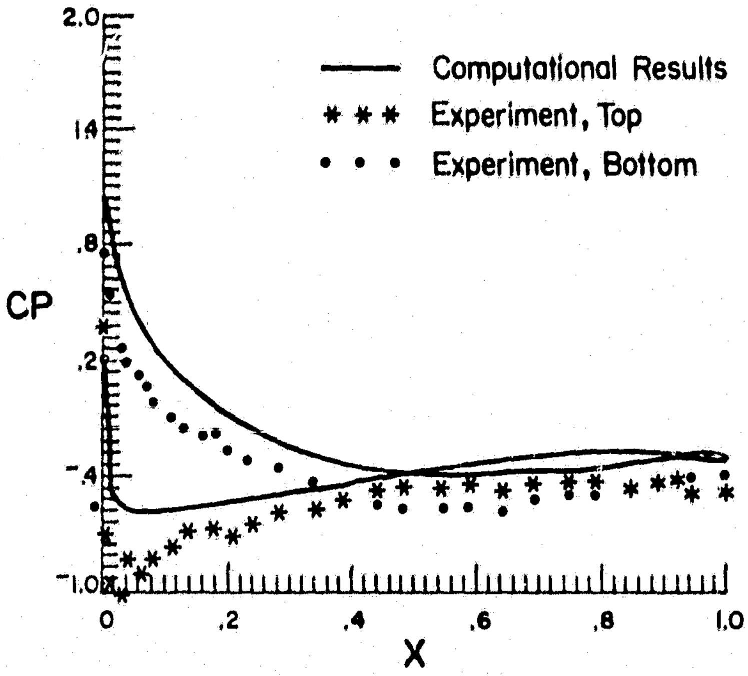

Figure 28. Pressure Distribution - Re = 40,000, α = 6°, t = 5.0

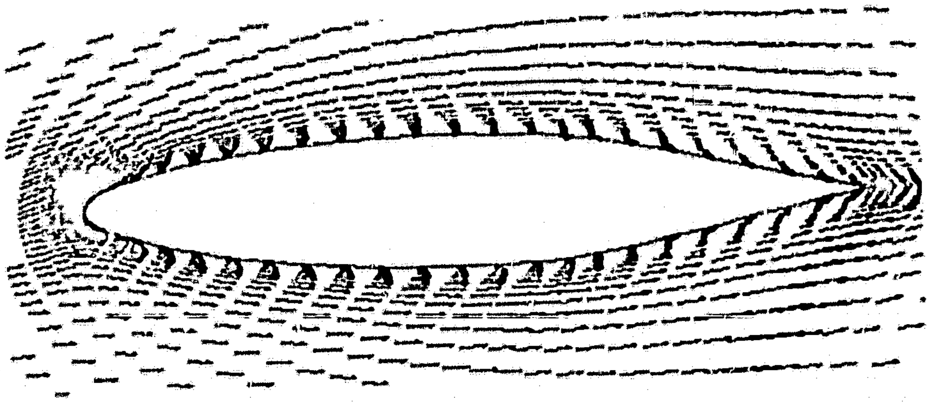

Figure 29. Velocity Field - Re = 40,000, α = 6°, t = 2.0

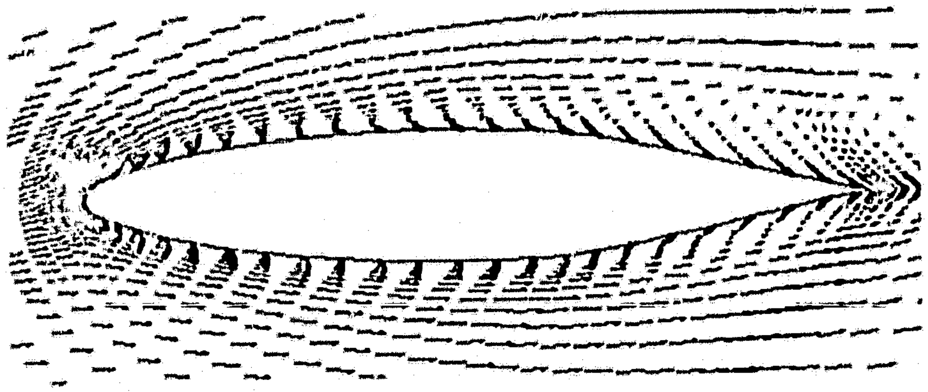

Figure 30. Velocity Field - Re = 40,000, α = 6°, t = 5.0

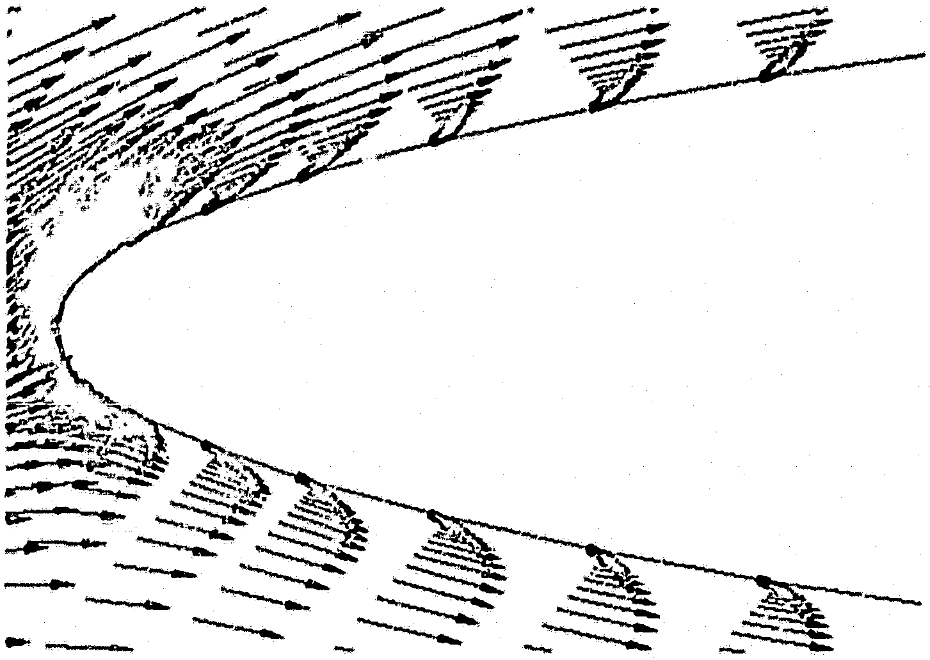

Figure 31. Leading-Edge Velocity Profiles - Re = 40,000, α = 6°, t = 2.0

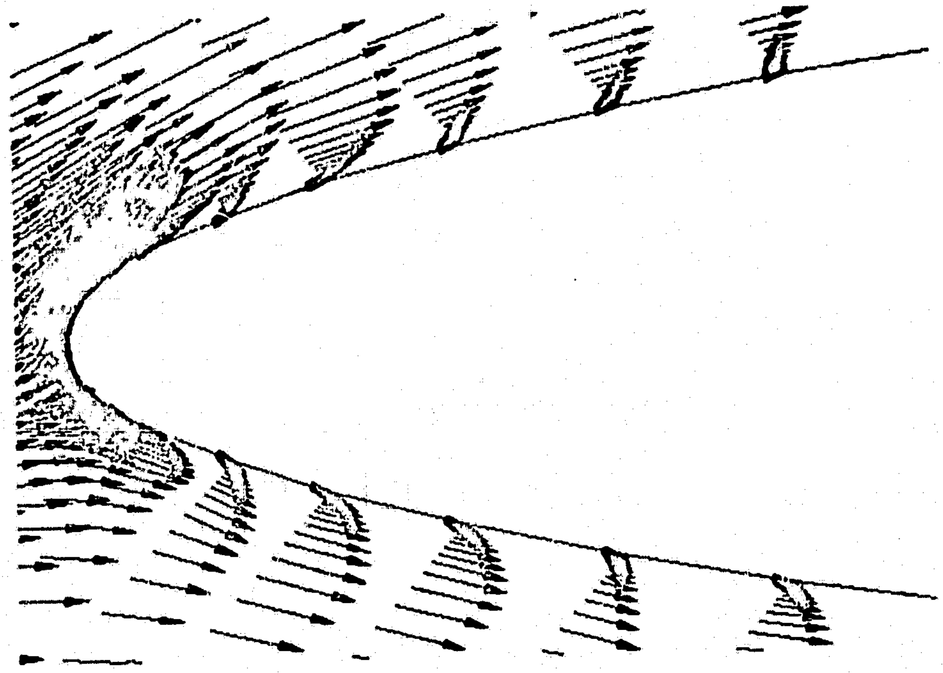

Figure 32. Leading-Edge Velocity Profiles - Re = 40,000, α = 6°, t = 5.0

L-2

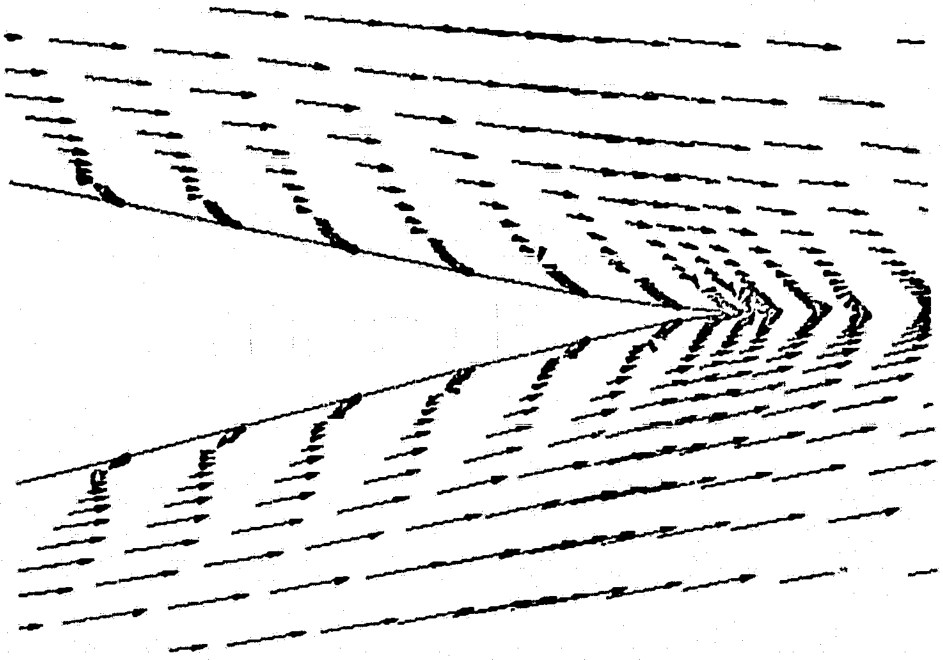

Figure 33. Trailing-Edge Velocity Profiles - Re = 40,000, $\alpha = 6°$, t = 2.0

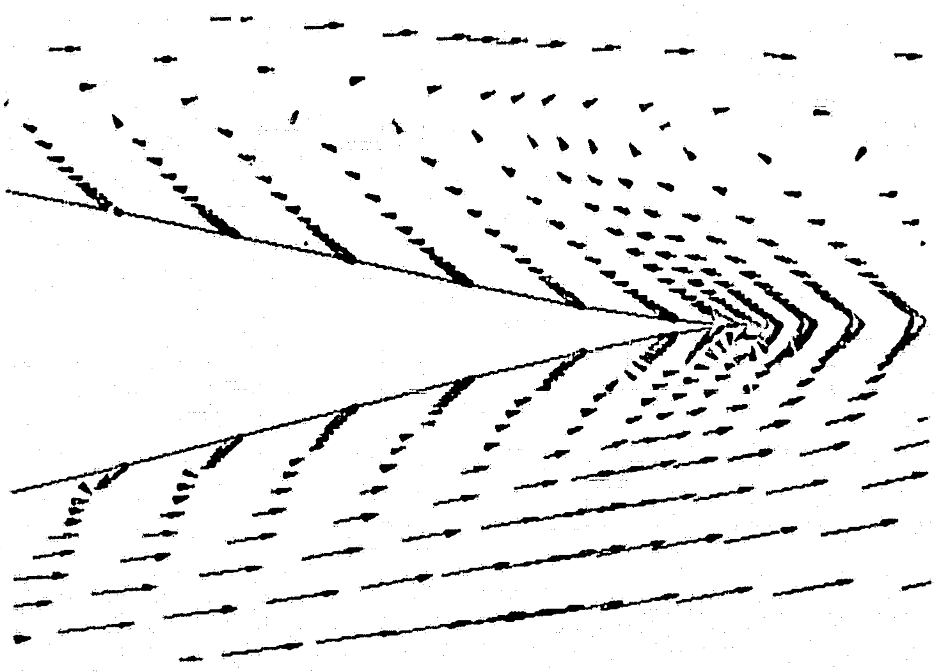

Figure 34. Trailing-Edge Velocity Profiles - Re = 40,000, α = 6°, t = 5.0

ORIGINAL PAGE IS
OF POOR QUALITY

APPENDIX A

FINITE-DIFFERENCE APPROXIMATIONS

The difference expressions listed below were used in discretizing the spatial derivatives in the main text (except where otherwise noted). The grid spacing in all cases is $\Delta\xi = \Delta\eta = 1$. Whenever the forms for the ξ- and η-derivatives are identical, only one form is given. The indices "i" and "j" denote ξ- and η-values, respectively.

Second-Order Central Differences:

$$f_{\xi} = \frac{1}{2}(f_{i+1} - f_{i-1}) \tag{A.1}$$

$$f_{\xi\xi} = f_{i+1} - 2f_{i} + f_{i-1} \tag{A.2}$$

$$(Wf_{\xi})_{\xi} = \frac{1}{4}(3W_{i+1} + W_{i-1})f_{i+1} - (W_{i+1} + W_{i-1})f_{i} + \frac{1}{4}(W_{i-1} + 3W_{i+1})f_{i+1} \tag{A.3}$$

$$f_{\xi\eta} = \frac{1}{4}(f_{i+1,j+1} - f_{i-1,j+1} - f_{i+1,j-1} + f_{i-1,j-1}) \tag{A.4}$$

$$(Wf_{\xi})_{\eta} = \frac{1}{4}[W_{i,j+1}(f_{i+1,j+1} - f_{i-1,j+1}) - W_{i,j-1}(f_{i+1,j-1} - f_{i-1,j-1})] \tag{A.5}$$

$$(Wf_{\eta})_{\xi} = \frac{1}{4}[W_{i+1,j}(f_{i+1,j+1} - f_{i+1,j-1}) - W_{i-1,j}(f_{i-1,j+1} - f_{i-1,j-1})] \tag{A.6}$$

First-Order One-Sided Differences:

$$\begin{aligned}(Zf_{\eta})_{\eta} = {} & \frac{1}{2}(3Z_{j+1} - Z_{j})f_{j+1} - 2Z_{j+1}f_{j} \\ & + \frac{1}{2}(Z_{j+1} + Z_{j})f_{j-1}\end{aligned} \tag{A.7}$$

$$
\begin{aligned}
(Xf_{\eta})_{\xi} + (Xf_{\xi})_{\eta} = {}& \frac{1}{2}(X_{i+1,j} + X_{i,j+1})f_{i+1,j+1} \\
& - \frac{1}{2}(X_{i-1,j} + X_{i,j+1})f_{i-1,j+1} \\
& - \frac{1}{2}(X_{i+1,j} + X_{ij})f_{i+1,j} + \frac{1}{2}(X_{i-1,j} + X_{ij})f_{i-1,j}
\end{aligned}
\tag{A.8}
$$

APPENDIX B

A DIFFERENCING PROBLEM

Cooper [8] points out that the same type of differencing should be used in the flow calculation as in the numerical calculation of the metric coefficients. For example, if central differences are used to calculate ξ_x and ξ_y , then the same should be used for u_ξ and v_ξ , and so on.

An additional problem has been encountered with respect to the viscous terms. Consider the two possible central-difference expressions for $(Zu_\eta)_\eta$

$$\begin{aligned}(Zu_\eta)_\eta &= \frac{1}{2}[(Zu_\eta)_{i,j+1} - (Zu_\eta)_{i,j-1}] \\ &= \frac{1}{4}(3Z_{i,j+1} + Z_{i,j-1})u_{i,j+1} \\ &\quad - (Z_{i,j+1} + Z_{i,j-1})u_{ij} \\ &\quad + \frac{1}{4}(3Z_{i,j-1} + Z_{i,j+1})u_{i,j-1}\end{aligned} \tag{B.1}$$

$$\begin{aligned}(Zu_\eta)_\eta &= (Zu_\eta)_{i,j+\frac{1}{2}} - (Zu_\eta)_{i,j-\frac{1}{2}} \\ &= \frac{1}{2}(Z_{i,j+1} + Z_{i,j})u_{i,j+1} \\ &\quad - \frac{1}{2}(Z_{i,j+1} + 2Z_{ij} + Z_{i,j-1})u_{ij} \\ &\quad + \frac{1}{2}(Z_{i,j-1} + Z_{ij})u_{i,j-1}\end{aligned} \tag{B.2}$$

For some reason, Eq. (B.1) works and (B.2) does not. The same problem applies to $(Wu_{\xi})_{\xi}$ and, of course, to similar terms involving the other velocity component v.

When Eq. (B.1) is used in the AF momentum solver, without ever calling the pressure solver, the results are stable and well-behaved (though erroneous next to the airfoil). On the other hand, if Eq. (B.2) is used, especially during the gradual start, oscillations arise in the velocities. This happens with or without the pressure solver, and the situation gets worse if the Reynolds number is reduced (just the opposite of what would be expected).

The reason for the instability with Eq. (B.2) is not clear. The metric quantities η_x and η_y use values of x and y at j+1 and j-1 but not at j. It is possible that the coefficients in the difference expression for $(Zu_{\eta})_{\eta}$ are restricted in the same way. In any case, the remedy is to use Eq. (B.1) , <u>not</u> Eq. (B.2).

BIBLIOGRAPHY

1. Chapman, D.R., "Computational Aerodynamics Development and Outlook," AIAA Journal, Vol. 17 (1979).

2. MacCormack, R.W., "A Rapid Solver for Hyperbolic Systems of Equations," Lecture Notes in Physics, Vol. 59, Springer-Verlag (1976).

3. Thompson, J.F., et al., "Automatic Numerical Generation of Body-Fitted Curvilinear Coordinate System for Field Containing Any Number of Arbitrary Two-Dimensional Bodies," J. of Comp. Physics, Vol. 15 (1974).

4. Beam, R.M., and Warming, R.F., "An Implicit Factored Scheme for the Compressible Navier-Stokes Equations," AIAA Paper 77-645, AIAA 3rd Computational Fluid Dynamics Conference (1977).

5. Briley, W.R., and McDonald, H., "An Implicit Numerical Method for the Multi-Dimensional Compressible Navier-Stokes Equations," Report M911393-6, United Aircraft Research Laboratories (1973).

6. Kutler, P., et al., "Supersonic Flow over Ablated Nosetips Using an Unsteady Implicit Numerical Procedure," AIAA Paper 78-213, AIAA 16th Aerospace Sciences Meeting (1978).

7. Steger, J.L., and Bailey, H.E., "Calculation of Transonic Aileron Buzz," AIAA Paper 79-0134, AIAA 17th Aerospace Sciences Meeting (1979).

8. Cooper, G.K., "An Approximate Factorization Solution of the Navier-Stokes Equations for Transonic Flow Using Body-Fitted Coordinates with Application to NACA 64A010 Airfoils," Ph.D. Dissertation, Mississippi State University (1980).

9. Steger, J.L., and Kutler, P., "Implicit Finite-Difference Procedures for the Computation of Vortex Wakes," AIAA Journal, Vol. 15 (1977).

10. Thompson, J.F., and Mastin, C.W., "Grid Generation Using Differential Systems Techniques," Numerical Grid Generation Techniques, NASA Conference Publication 2166 (1980).

11. Roache, P.J., Computational Fluid Dynamics, Hermosa Publishers (1976).

12. Steger, J.L., "Implicit Finite Difference Simulation of Flow about Arbitrary Geometries with Application to Airfoils," AIAA Paper 77-665, AIAA 10th Fluid & Plasmadynamics Conference (1977).

13. Hirt, C.W., and Harlow, F.H., "A General Corrective Procedure for the Numerical Solution of Initial Value Problems," Journal of Computational Physics, Vol. 2 (1967).

14. Baldwin, B.S., and Lomax, H., "Thin Layer Approximation and Algebraic Model for Separated Turbulent Flows," AIAA Paper 78-257, AIAA 16th Aerospace Sciences Meeting (1978).

15. Thompson, J.F., Personal Communication, Dept. of Aerospace Engineering, Mississippi State University, Mississippi State, Mississippi (1981).

16. Mueller, T.J., Personal Communication, Dept. of Aerospace and Mechanical Engineering, University of Notre Dame, Notre Dame, Indiana (1981).